



New plume comparison metrics for the inversion of passive gases emissions

Pierre J. Vanderbecken¹, Joffrey Dumont Le Brazidec¹, Alban Farchi¹, Marc Bocquet¹, Yelva Roustan¹,
Élise Potier², and Grégoire Broquet²

¹CEREA, École des Ponts and EDF R&D, Île-de-France, France

²Laboratoire des Sciences du Climat et de l'Environnement, LSCE-IPSL (CEA-CNRS-UVSQ), Université Paris-Saclay,
91191 Gif-sur-Yvette, France

Correspondence: Vanderbecken Pierre (pierre.vanderbecken@enpc.fr)

Abstract. In the next few years, numerous satellites with high-resolution instruments dedicated to the imaging of atmospheric gaseous compounds will be launched, to finely monitor emissions of greenhouse gases and pollutants. Processing the resulting images of plumes from cities and industrial plants to infer the emissions of these sources can be challenging. In particular traditional atmospheric inversion techniques, relying on objective comparisons to simulations with atmospheric chemistry transport models may poorly fit the observed plume due to modelling errors rather than due to uncertainties in the emissions.

The present article discusses how these images can be properly compared to simulated concentrations to limit the weight of modelling errors due to the meteorology used to analyse the images. For such comparisons, the usual pixel-wise \mathcal{L}_2 norm may not be a good option, because it is subject to the double penalty issue inherent to its local definition. This issue is characterised by a mutation of any position shift into significant amplitude discrepancies. To circumvent this issue, we propose to either provide an upstream correction of the position misfit between the observed and simulated plumes in the usual \mathcal{L}_2 norm or to use a non-local metric based on the optimal transport theory, such as the Wasserstein distance.

All the metrics are evaluated using first a catalogue of analytical plumes and then more realistic plumes simulated with a mesoscale Eulerian atmospheric transport model, with an emphasis on the sensitivity of the metrics to position mismatch and the concentration values within the plumes. As expected, the metrics with the upstream correction are found to be less sensitive to position errors in both analytical and realistic conditions. Furthermore, in realistic cases, we evaluate the weight of changes in the norm and the direction of the four-dimensional wind fields in our metric values. This comparison highlights the link between differences in the synoptic-scale winds direction and position error. It is found that discrepancies between two plume images due to wind direction errors in the meteorological conditions are less penalised by our new metrics with the upstream correction than without, thus avoiding the double penalty issue.



1 Introduction

Near real-time monitoring of atmospheric gaseous compounds at the scale of power plants, cities, regions and countries would allow decision makers to track the effectiveness of emission reduction policies in the context of climate change mitigation (Horowitz, 2016) or other voluntary emission reduction efforts. Inventories of emitted atmospheric gaseous compound are
25 diverse in scale (Janssens-Maenhout et al., 2019; Kuenen et al., 2014) and methodology. The elaboration of comprehensive inventories generally combines various approaches based on a complex mixture of measurement techniques, database elaboration and numerical modelling. Despite the use of quality assurance and control verifications (Calvo Buendia et al., 2019a, b) the emissions fluxes can bear large uncertainties, depending on the species, on the countries or on the spatial scale (Cai et al., 2019; Hergoualc'h et al., 2021; Meinshausen et al., 2009; Pison et al., 2018; Solazzo et al., 2021). Furthermore, the delay between
30 the emissions and the release of the corresponding inventory could be important due to a large amount of data to gather and aggregate. Even when the inventories are known to be accurate, they currently do not fulfil the need for real-time monitoring of the emissions at a regional scale. By observing from space the plumes of gases downwind of large cities and industrial plants, and atmospheric signals at a few to several hundred km scales, the new generation of high-resolution spectro-imagery may help address this need (Veefkind et al., 2012; Broquet et al., 2018). For instance, the future CO₂M mission will provide images of
35 CO₂ concentrations at a resolution of almost two kilometres square, which will enable the observation of urban scale pollutant plumes (Brunner et al., 2019; Kuhlmann et al., 2019, 2020). These new images can be directly used through fast methods to quantify the mean emissions of sources (Varon et al., 2018, 2020; Hakkarainen et al., 2021). These fast methods require only the images to provide an estimation of the emissions, but, they do so, by assuming either simplified chemistry, transport or temporal variations of the emissions.

40 Here we focus on the use of such images to update the emissions sources on a smaller time scale. This can be done using an inverse method relying on comparisons between the images and the predictions of a chemical transport model (CTM). A better match between the observed concentration fields and the simulated one will be the result of a more accurate source. However, the CTM prediction is bounded by the meteorological conditions used. It takes as inputs temperature, pressure, winds, cloud cover fields, etc. Usually, these atmospheric fields are provided by predictions previously obtained with mesoscale numerical
45 weather prediction models (Lian et al., 2018). The estimated atmospheric fields come with uncertainties, which in turn yield uncertainties in the simulated concentration fields. Within the inverse technique, the concentration fields derived from satellites and CTM models are usually compared pixel-wise. However, the relative weight of the meteorological uncertainties within the comparison between observation and simulation cannot be easily removed through pixel-wise comparison, and thus the emissions inventories that estimate our sources could be erroneously updated due to the approximated meteorology used in the
50 simulations. This issue is shared in other fields (Dumont Le Brazidec et al., 2021; Farchi et al., 2016; Keil and Craig, 2007). Here, our view is that meteorology drives the position error between the plume observed and the plume simulated by the CTM. Thus our main goal is then to define a metric for the comparison that level down the position error to reduce the weight of meteorology uncertainties within the inversion.



To control the weight of position uncertainties in a comparison, several methods have been developed. They can be classified according to their basic principles. A first category corresponds to methods that project the image on a specific basis using either droplet or analogous decomposition to keep only the critical components of the field (Briggs and Levine, 1997). A second method corresponds to the relaxation of the pixel-wise comparison and hence to the smoothing of discrepancies due to the shifting between the fields (Ebert, 2008; Amodei et al., 2009). A third category is based on object, feature description of the image, their identification and their comparison using image processing method (Davis et al., 2006; Lack et al., 2010; Davis, 2019). Such a method stresses the differences in terms of simple patterns and objects between the images and does not provide a straightforward evaluation of the gradient with respect to the inputs of the model which is needed for inverse modelling. The fourth category is based on an upstream distortion of the images to take into account the position error (Gilleland et al., 2009; Gilleland, 2021; Hoffman et al., 1995; Hoffman and Grassotti, 1996). These approaches were designed to score and evaluate the quality of a given weather forecast with better interpretability. We will follow this idea of a moving field and apply it to our problem of plume comparison. Our options are either to correct upstream the simulated concentration field or to adopt an optimal transport metric that weights the movement to superimpose the observed concentration field with the simulated one.

The objective of this paper is to develop a simple and efficient metric for urban-scale plume images which can level down the difference due to the meteorology while fitting into an inverse framework (following Feyeux et al., 2018; Tamang et al., 2022). Even though the methods could be used for other gaseous compounds, reactive atmospheric gaseous have a more complex transport due to chemistry. For the sake of simplicity, we will consider the CO_2 since it is a passive tracer. Several metric candidates are introduced and compared. From the baseline local \mathcal{L}_2 norm, a new metric with an upstream non-local correction of position errors is described in section 2. In section 3, going further away from the local comparison, we use the optimal transport theory to define the Wasserstein distance between two plumes and then to build a new metric freed from position errors. The different metrics are then evaluated and compared on a database of analytical two-dimensional Gaussian puff cases in section 4. The metrics are then compared on a realistic database of CO_2 plumes from a German power plant in section 5. For both databases, the images and the simulations are computed using the same model, which allows us to monitor the discrepancies seen by the metrics. In section 6 we describe the dependence of the four metrics on meteorology, before concluding in section 7.

2 Local metrics and illustration of double penalty issue using analytical plumes

In this section, we start by introducing the notation in section 2.1 and then the Gaussian puff model used to simulate the plumes in the analytical experiments in section 2.2. Furthermore, we assume that the plumes are already detected and separated from the background noise and instrumental noise. These steps bring challenges that are outside the scope of this article. The \mathcal{L}_2 norm is then defined in section 2.3, with an emphasis on the double penalty issue. To deal with the double penalty issue associated with the family of pixel-wise metrics such as the \mathcal{L}_2 norm, a second metric is proposed in section 2.4.



85 2.1 Discrete and continuous representation of an image

In the present article, we focus on two-dimensional images – typically of the total column of CO₂ concentration, or of ground level concentration field –, full (no mask due to filtered data or clouds), with a discretisation of N pixels. An image can hence be represented by a vector $\mathbf{x} = (x_1, \dots, x_N)^\top \in \mathbb{R}^N$.

It is also possible to obtain a continuous representation of the image using an interpolation (e.g. bilinear). In this case, the
90 image is represented by a two-dimensional field $X : \mathbb{E} \rightarrow \mathbb{R}$ defined on a finite domain $\mathbb{E} \subset \mathbb{R}^2$. Without loss of generality, we can assume that $\mathbb{E} = [0, 1]^2$. Furthermore, the two-dimensional field X can be extended to \mathbb{R}^2 by using zero padding outside the original domain \mathbb{E} . If needed, a smooth transition from X to 0 can be included to avoid a sharp gradient at the boundaries of the original domain \mathbb{E} .

For each metric definition, we will use either the discrete or the continuous representation of the images, but this will be
95 explicitly mentioned.

2.2 Analytical plumes

Our Gaussian puff model is a simplified model of a concentration field (e.g. concentration at a given altitude or total column concentration in specific conditions). It has the advantage to yield analytical expressions for the Wasserstein metrics (see section 3). It is also a relevant case in transport modelling: the transport of a three-dimensional Gaussian puff is a simplified
100 model to estimate the transport of non-reactive pollutants (Korsakissok and Mallet, 2009; Seigneur, 2019). A set of Gaussian puffs is used extensively in the following sections to illustrate and evaluate the metric candidates.

In the Gaussian puff model, we assume that X is proportional to the probability density function (pdf) of the normal distribution $\mathcal{N}(\boldsymbol{\mu}, \boldsymbol{\Sigma})$:

$$X(\mathbf{x}) \propto \frac{1}{\sqrt{(2\pi)^2 |\boldsymbol{\Sigma}|}} \exp \left[-\frac{1}{2} (\mathbf{x} - \boldsymbol{\mu})^\top \boldsymbol{\Sigma}^{-1} (\mathbf{x} - \boldsymbol{\mu}) \right], \quad (1)$$

105 where $\boldsymbol{\mu}$ and $\boldsymbol{\Sigma}$ are the mean and the covariance matrix, respectively. The operator $|\cdot|$ is the determinant for square matrices. Also note that, since the covariance matrix $\boldsymbol{\Sigma}$ is positive definite, it can be factored as follows:

$$\boldsymbol{\Sigma} = \mathbf{R}(\theta) \boldsymbol{\Delta} \mathbf{R}(\theta)^\top, \quad (2)$$

where $\mathbf{R}(\theta)$ is the rotation matrix of angle θ , the angle between the principal axis of the Gaussian and the x -axis, and where $\boldsymbol{\Delta}$ is a diagonal matrix with the variance along the two principal axes of the Gaussian. Two examples of puffs based on the
110 Gaussian puff model are provided in Figure 1, panels (b) and (c).

2.3 The \mathcal{L}_2 norm and the double penalty issue

To compare two concentration fields, one can see to what extent the fields overlap. This provides a pixel-wise (i.e. local) assessment of the discrepancies. The \mathcal{L}_2 norm is then defined as the sum of the squared discrepancies. More specifically, the

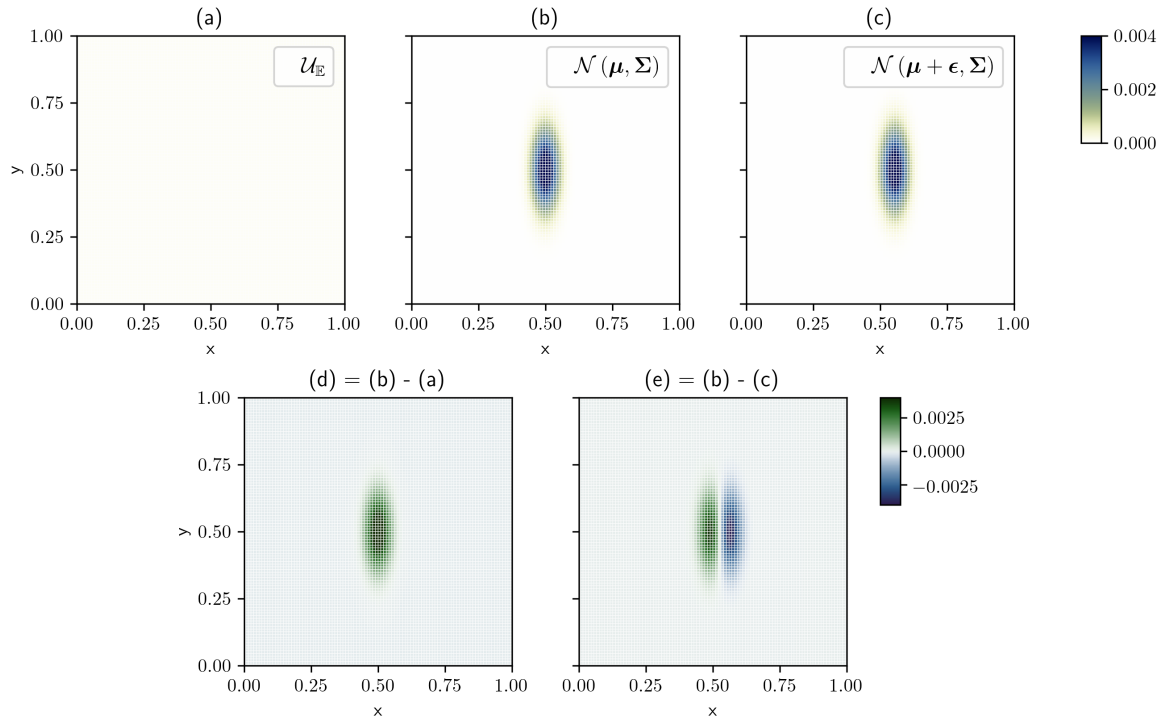


Figure 1. Example of pixel wise comparison. (a) Uniform concentration. (b) First Gaussian puff. (c) Second Gaussian puff, similar to (b) but shifted along the x axis by $\epsilon = 0.054$. (d) Discrepancies between the concentration fields (b) and (a). (e) Discrepancies between the concentration fields (b) and (c).

\mathcal{L}_2 norm d between two concentration fields X_A and X_B is defined as

$$115 \quad d(X_A, X_B) \triangleq \sqrt{\frac{\int_{\mathbb{R}^2} [X_A(\mathbf{x}) - X_B(\mathbf{x})]^2 d\mathbf{x}}{\int_{\mathbb{R}^2} \mathbf{1}_E d\mathbf{x}}}, \quad (3)$$

or

$$120 \quad d(\mathbf{x}_A, \mathbf{x}_B) \triangleq \sqrt{\frac{1}{N} \sum_{n=1}^N (x_{A,n} - x_{B,n})^2}, \quad (4)$$

in the discrete case, where \mathbf{x}_A and \mathbf{x}_B are the two concentration vectors corresponding to the concentration fields X_A and X_B . In the limit of an higher and higher resolution, the discrete formulation should converge towards the continuous formulation.

To identify the origin of the discrepancies, Feyeux et al. (2018) propose to split the difference between two fields into two categories: the position error and the amplitude error. A position error occurs when the two compared plumes are not located in the same place in the images. An amplitude error occurs when the two compared plumes are in the same place in the images but



Table 1. Comparison between the distances for the example in Figure 1. d is the \mathcal{L}_2 norm, d_F the \mathcal{L}_2 norm with upstream position correction as defined in section 2.4, w the Wasserstein distance (section 3.1) and w_F the Wasserstein distance with upstream position correction (section 3.4). The results are not provided with units since it depends on the metric used. The metrics d and d_F share the same units while w and w_F share an another one.

Distance	(a) versus (b)	(b) versus (c)
d	48.80×10^{-5}	48.80×10^{-5}
d_F	48.82×10^{-5}	11.59×10^{-8}
w	32.68×10^{-2}	52.90×10^{-3}
w_F	31.75×10^{-2}	93.13×10^{-11}

locally their pixels do not have the same values. With the \mathcal{L}_2 pixel-wise norm, all the discrepancies are seen as local amplitude errors. This property is illustrated in Figure 1, where a uniform concentration field $\mathcal{U}_{\mathbb{E}}$ is compared to two Gaussian puffs shifted by $\epsilon = 0.054$ along the x axis with respect to each other¹. The values of the distance are reported in Table 1. In this case, a small position error is penalised by d as much as an absence of plume: this is the so-called double penalty issue. The idea is that, instead of considering the cost of the translation, the metric adds the cost to set to zero all pixels from the first Gaussian puff to the cost to enhance the pixels at the translated location.

In the following sections, we further extend the classification of Feyeux et al. (2018) by splitting the amplitude error into two sub-categories: the scale error and the shape error. The scale error corresponds to the difference in total amplitude between two shape-matching fields. More practically, the difference between the sum of the compared image pixels. The shape error corresponds to the difference between the isocontours after removal of the scale error (i.e. normalisation) and position error (i.e. when both centres of mass and principal axes are superimposed) fields.

2.4 Local metric with non-local upstream position correction

We propose to address the double penalty issue while still relying on the \mathcal{L}_2 norm by applying an upstream correction of the position error to d . The position error can be seen as a combination of an orientation and a translation error. The orientation error corresponds to the differences that could be reduced by a rotation applied to two concentration fields sharing the same centre of mass location that maximises their overlapping. The translation error corresponds to the difference that could be reduced by a translation applied to two concentration fields.

The new distance is defined in a way that involves finding the rotation and translation that minimise d . The idea is that the rotation should cancel the orientation error and the translation should cancel the translation error. Let us consider the plane transformation \mathbf{F} defined as follows:

$$\mathbf{F}(\mathbf{x}) = \mathbf{x}_0 + \mathbf{x}_t + \mathbf{R}(\theta)[\mathbf{x} - \mathbf{x}_0], \quad (5)$$

¹For this specific value of ϵ , the d distance between $\mathcal{U}_{\mathbb{E}}$ and the first plume is similar to the d distance between the two plumes.



which corresponds to a translation of vector $\mathbf{x}_t = (x_t, y_t)^\top$, followed by a rotation of angle θ and of centre $\mathbf{x}_0 + \mathbf{x}_t$, where
 145 $\mathbf{x}_0 = (x_0, y_0)^\top$ is the position of the centre of mass of the plume before the transformation. The transformation \mathbf{F} depends on
 three parameters: (x_t, y_t, θ) . Note that this is an isometry of the plane. The optimal transformation should minimise

$$\mathcal{J}(x_t, y_t, \theta) \triangleq d^2(X_A, X_B \circ \mathbf{F}), \quad (6a)$$

$$= \int_{\mathbb{R}^2} [X_A(\mathbf{x}) - X_B(\mathbf{F}(\mathbf{x}))]^2 d\mathbf{x} / \int_{\mathbb{R}^2} \mathbf{1}_{\mathbb{E}} d\mathbf{x}. \quad (6b)$$

However, this cost function is constant for any transformation that moves all the mass of the B -plume outside the domain $\mathbb{E} =$
 150 $[0, 1]^2$, where by construction X_B is null. This would make the minimisation very difficult with gradient-based optimisation
 methods. For this reason, we add the following regularisation term to the cost function

$$\rho(x_t, y_t) \triangleq \begin{cases} (x_t^2 + y_t^2 - \frac{1}{2})^3 & \text{if } (x_t^2 + y_t^2) > 1/2, \\ 0 & \text{else,} \end{cases} \quad (7)$$

to penalise any transformation that moves the B -plume outside the domain \mathbb{E} . This regularisation does not affect the location
 of the minima of d_F . The final cost function is

$$155 \quad \mathcal{J}(\theta, x_t, y_t) \triangleq \alpha d^2(X_A, X_B \circ \mathbf{F}) + \beta \rho(x_t, y_t) \quad (8)$$

where α is set to the average mass of the A - and B -plumes, and β is set by trial and error to 10^4 . In practice, the cost function
 \mathcal{J} can be minimised with the L-BFGS algorithm (Nocedal and Wright, 2006) that is based on the gradient of \mathcal{J} with respect to
 all three parameters θ, x_t, y_t , whose expression is given in appendix B. To compute the gradient, the spatial partial derivatives
 of the concentration field X_B are needed. Hence, to ensure the continuity of the partial derivatives, we use a second-order
 160 bivariate spline interpolation to define the continuous concentration field X_B from its original image \mathbf{x}_b . In order to avoid any
 issue due to the local non-convexity of the problem, we also provide a specific initialisation to the minimisation algorithm. The
 initial translation is then computed using the two centres of mass. Then we do orthogonal regressions to compute the principal
 axes of both X_A and X_B . The initial θ is the angle between these axes.

Finally, with the optimal transformation \mathbf{F}^* , i.e. the one that minimises \mathcal{J} defined by (8), the new distance, called d_F , is
 165 defined by

$$d_F(X_A, X_B) \triangleq d(X_A, X_B \circ \mathbf{F}^*). \quad (9)$$

For the example of Figure 1, the values of d_F are reported in Table 1 and can be compared to the values of d . In the second
 case (distance between the two Gaussian puffs), d_F is close to zero. The residual value is due to the finite resolution of the
 images. In the first case (distance between the Gaussian puff and the uniform concentration), d_F stays similar to d because any
 170 transformation \mathbf{F} that keeps the plume in the domain is optimal.



3 Metrics based on optimal transport theory

In this section, we introduce the Wasserstein distance, the distance of the optimal transport, as a non-local alternative to the pixel-wise \mathcal{L}_2 norm.

3.1 Optimal transport and the Wasserstein distance

175 The optimal transport theory was first introduced in the XVIIth century by Monge in his famous memoir (Monge, 1781). It is based on the idea that there exists a transport plan to move masses that minimises a given cost of transport. A wider view of the problem was proposed by Kantorovich (Kantorovich, 1942) using a probabilistic approach. The field has finally regained popularity in the last few decades, in particular with the generalisation by Villani (2009).

180 In this section, we follow the Kantorovich approach, which means that we will use the discrete representation (see section 2.1). Moreover, the theory is defined only for vectors whose coefficients are non-negative and sum up to one. While the first condition is satisfied in our case (because we work with images of pollutant concentration), the second is not. Therefore, in the following instead of working with the concentration vectors \mathbf{x}_A and \mathbf{x}_B , we will work with their normalised counterparts $\hat{\mathbf{x}}_A$ and $\hat{\mathbf{x}}_B$:

$$\hat{\mathbf{x}} \triangleq \frac{\mathbf{x}}{\mathbf{x}^\top \mathbf{1}}, \quad (10)$$

185 where $\mathbf{1} \in \mathbb{R}^N$ is the vector full of ones and $\mathbf{x} \in \mathbb{R}^N$ is either \mathbf{x}_A or \mathbf{x}_B .

The set of couplings \mathbf{P} between $\hat{\mathbf{x}}_A$ and $\hat{\mathbf{x}}_B$ is defined by

$$\mathcal{U}(\hat{\mathbf{x}}_A, \hat{\mathbf{x}}_B) \triangleq \{ \mathbf{P} \in \mathbb{R}_+^{N \times N} : \mathbf{P}\mathbf{1} = \hat{\mathbf{x}}_A \text{ and } \mathbf{P}^\top \mathbf{1} = \hat{\mathbf{x}}_B \}. \quad (11)$$

Note that $\mathcal{U}(\hat{\mathbf{x}}_A, \hat{\mathbf{x}}_B)$ is not empty because $\mathbf{P} = \hat{\mathbf{x}}_A \hat{\mathbf{x}}_B^\top$ is a coupling between $\hat{\mathbf{x}}_A$ and $\hat{\mathbf{x}}_B$. The cost of a coupling $\mathbf{P} \in \mathcal{U}(\hat{\mathbf{x}}_A, \hat{\mathbf{x}}_B)$ is defined by

$$190 \quad \mathcal{J}(\mathbf{P}) = \sum_{i,j=1}^N C_{i,j} P_{i,j}, \quad (12)$$

where $C_{i,j} \geq 0$ is the (i,j) -element of the cost matrix \mathbf{C} penalising the transport between $\hat{\mathbf{x}}_A$ and $\hat{\mathbf{x}}_B$. Here, it is chosen to be the square of the Euclidean distance between the i -th and j -th pixels of the original image. For this specific choice, the cost function \mathcal{J} defined by eq. (12) has a minimum, which is obtained for a unique coupling \mathbf{P}^* . The Wasserstein distance, the distance of the optimal transport, is then defined by

$$195 \quad w(\hat{\mathbf{x}}_A, \hat{\mathbf{x}}_B) = \sqrt{\sum_{i,j=1}^N C_{i,j} P_{i,j}^*} \quad (13)$$

and it is actually a distance according to the mathematical definition. The proofs of these statements can be found in optimal transport textbooks (e.g., Villani, 2009).

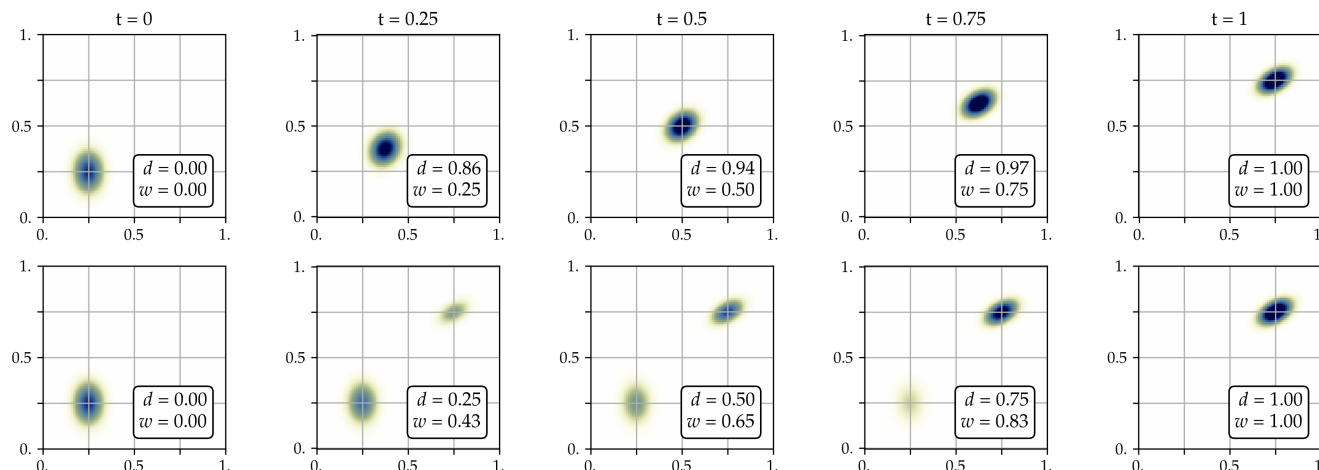


Figure 2. Comparison between the optimal transport interpolation (top panels) and the linear interpolation (bottom panels). In both cases, we interpolate between two puffs using a pseudo time ranging from $t = 0$ (interpolated puff equal to the first puff) to $t = 1$ (interpolated puff equal to the second puff). In each panel, the legend indicates both the w and d distances between the first puff and the interpolated puff, normalised by the distance between the first and second puff. By construction, for the optimal transport interpolation w linearly grows with t , and for the linear interpolation d linearly grows with t .

Two interesting properties of the Wasserstein distance can be highlighted. First, this metric is defined for normalised vectors only. This means in our case that the difference in total mass between two images is entirely ignored. Alternative solutions have been proposed to take into account this difference, e.g. the one proposed by Farchi et al. (2016) or the use of unbalanced optimal transport (Chizat et al., 2018), but this is beyond the scope of the present study.

Second, following Benamou and Brenier (2000), it is possible to define an optimal transport interpolation between \hat{x}_A and \hat{x}_B . This optimal transport interpolation can help us visualise the idea of vicinity according to w . An example is shown in Figure 2 for two Gaussian puffs. In the case of the optimal transport interpolation, the w distance between the first puff and the interpolated puff is linearly growing (by the construction of the interpolation), while the increase of the d distance is at first very steep. In some sense, this behaviour was expected since the first puff and the interpolated puff are quickly separated from each other. In the case of the linear interpolation, the same phenomenon happens: the d distance is linearly growing (by the construction of the interpolation), while the increase of the w is steeper, but not as steep as the increase of d in the first case. This shows that the Wasserstein distance w is a softer metric than the distance d and evaluates discrepancies more fairly especially those due to the position error.

3.2 Sinkhorn's algorithm

To compute the Wasserstein distance, we have to determine the optimal coupling matrix \mathbf{P}^* by minimising \mathcal{J} defined by eq. (12). The convexity of the cost function \mathcal{J} is not guaranteed, thus it is usual (see, e.g., Peyré and Cuturi, 2019, and



references therein) to add the following entropic regularisation:

$$215 \quad \mathcal{H}(\mathbf{P}) \triangleq - \sum_{i,j=1}^N P_{i,j} (\ln P_{i,j} - 1). \quad (14)$$

The objective function to minimise becomes:

$$\mathcal{J}^\epsilon(\mathbf{P}) = \sum_{i,j=1}^N P_{i,j} C_{i,j} + \epsilon \sum_{i,j=1}^N P_{i,j} (\ln P_{i,j} - 1), \quad (15)$$

under the same constraint $\mathbf{P} \in \mathcal{U}(\hat{\mathbf{x}}_A, \hat{\mathbf{x}}_B)$. The solution of the regularised problem is an approximation of the Wasserstein distance. When $\epsilon \rightarrow 0$ it converges toward the exact value of the Wasserstein distance $w(\hat{\mathbf{x}}_A, \hat{\mathbf{x}}_B)$ and when $\epsilon \rightarrow \infty$ the optimal
 220 coupling matrix converges toward $\mathbf{P} = \hat{\mathbf{x}}_A \hat{\mathbf{x}}_B^\top$.

It is possible to show that minimising eq. (15) is equivalent to minimising the Kullback–Leibler divergence between $\mathbf{P} \in \mathcal{U}(\hat{\mathbf{x}}_A, \hat{\mathbf{x}}_B)$ and the Gibbs kernel $\mathbf{K} = \exp(-\mathbf{C}/\epsilon)$, where the exponential is applied entry-wise, which is given by

$$\text{KL}(\mathbf{P}|\mathbf{K}) = \sum_{i,j=1}^N P_{i,j} \ln \left(\frac{P_{i,j}}{K_{i,j}} \right) - P_{i,j} + K_{i,j}. \quad (16)$$

The advantage of this formulation is that this problem is known to admit a unique solution which is the projection of the Gibbs
 225 kernel \mathbf{K} onto $\mathcal{U}(\hat{\mathbf{x}}_A, \hat{\mathbf{x}}_B)$. This unique solution can be written

$$\mathbf{P} = \mathbf{u}^\top \mathbf{K} \mathbf{v}, \quad (17)$$

where \mathbf{u} and \mathbf{v} are vectors with positive or null entries satisfying

$$\mathbf{u} \circ (\mathbf{K} \mathbf{v}) = \hat{\mathbf{x}}_A, \quad (18a)$$

$$\mathbf{v} \circ (\mathbf{K}^\top \mathbf{u}) = \hat{\mathbf{x}}_B. \quad (18b)$$

230 In these equations, \circ is the Schur/Hadamard (i.e. entry-wise) product in \mathbb{R}^N .

The (\mathbf{u}, \mathbf{v}) factorisation is unique and can be easily found using the iterative update scheme proposed by Sinkhorn, where the l -th update is given by

$$\mathbf{u}^{(l+1)} = \frac{\hat{\mathbf{x}}_A}{\mathbf{K} \mathbf{v}^{(l)}}, \quad (19a)$$

$$\mathbf{v}^{(l+1)} = \frac{\hat{\mathbf{x}}_B}{\mathbf{K}^\top \mathbf{u}^{(l+1)}}, \quad (19b)$$

235 where \div is the entry-wise division in \mathbb{R}^N .

3.3 Log-formulation of Sinkhorn’s algorithm

Sinkhorn’s algorithm provides a simple and quick solution to the optimal transport problem. However, this formulation raises technical issues. The first is that for small values of ϵ – which is what we are aiming for to be as close as possible to the true



optimal transport solution – the algorithm converges slowly². To accelerate the convergence, we use a high value of ϵ and progressively decrease it whenever (\mathbf{u}, \mathbf{v}) has converged. We will use this technique in our experiments.

Another numerical issue appears when ϵ is small compared to the entries of \mathbf{C} . In this case, \mathbf{u} , \mathbf{v} , and \mathbf{K} explode and cannot be computed with finite numerical precision. To address this issue, we adopt the log-Sinkhorn algorithm proposed by Peyré and Cuturi (2019), which is presented in the following lines.

Let us introduce \mathbf{f} and \mathbf{g} which are related to \mathbf{u} and \mathbf{v} by

$$u_i = \exp(f_i/\epsilon), \quad (20a)$$

$$v_j = \exp(g_j/\epsilon). \quad (20b)$$

Instead of updating (\mathbf{u}, \mathbf{v}) with Sinkhorn iteration eq. (19), we update (\mathbf{f}, \mathbf{g}) using

$$f_i^{(l+1)} = -\epsilon \ln \left[\sum_{j=1}^N \exp \left\{ \frac{f_i^{(l)} + g_j^{(l)} - C_{i,j}}{\epsilon} \right\} \right] + f_i^{(l)} + \epsilon \ln \hat{x}_{A,i}, \quad (21a)$$

$$g_j^{(l+1)} = -\epsilon \ln \left[\sum_{i=1}^N \exp \left\{ \frac{f_i^{(l+1)} + g_j^{(l)} - C_{i,j}}{\epsilon} \right\} \right] + g_j^{(l)} + \epsilon \ln \hat{x}_{B,j}. \quad (21b)$$

Combining the log-Sinkhorn algorithm while decreasing ϵ is not straightforward, because there are a lot of numerical decisions to make: intermediate and final values of ϵ , convergence criteria, etc. After several tests, we ended up with Algorithm 1, which we found to be a good trade-off between speed and accuracy. The value of ϵ is progressively decreased from 1 to 10^{-5} : each time the convergence criterion is met, ϵ is reduced by a factor of 10. In our case, the convergence criterion is met when the relative difference between the former and the current value of the Wasserstein distance falls below $\zeta = 5 \times 10^{-4}$. In addition, we set a maximum number of Sinkhorn iterations of 200 per value of ϵ to keep the computational cost under control. Finally, note that, for a given ϵ , one can try to accelerate the convergence by using the averaging step proposed in Chizat et al. (2018) but this is beyond the scope of the present study.

3.4 Gaussian approximation and upstream correction

Following the derivation of section 2.4, we want to apply the same upstream correction of the position error to the Wasserstein distance w . However, this would require the gradient of the Wasserstein distance w with respect to each one of its inputs. The computation is not straightforward, even taking into account the log-Sinkhorn formulation developed in section 3.3. For this reason, we will use the Gaussian approximation, for which the Wasserstein distance has an analytical formula.

More specifically, we assume that we have two continuous concentration fields X_A and X_B that follow the Gaussian puff model:

$$X_A(\mathbf{x}) = \frac{1}{\sqrt{(2\pi)^2 |\boldsymbol{\Sigma}_A|}} \exp \left[-\frac{1}{2} (\mathbf{x} - \boldsymbol{\mu}_A)^\top \boldsymbol{\Sigma}_A^{-1} (\mathbf{x} - \boldsymbol{\mu}_A) \right], \quad (22a)$$

$$X_B(\mathbf{x}) = \frac{1}{\sqrt{(2\pi)^2 |\boldsymbol{\Sigma}_B|}} \exp \left[-\frac{1}{2} (\mathbf{x} - \boldsymbol{\mu}_B)^\top \boldsymbol{\Sigma}_B^{-1} (\mathbf{x} - \boldsymbol{\mu}_B) \right], \quad (22b)$$

²The convergence speed is measured here by the number of iterations.



Algorithm 1 Log-Sinkhorn algorithm with decreasing ϵ to compute the Wasserstein distance.

Parameters: $\epsilon_0 = 1$, $\epsilon_* = 10^{-5}$, $\delta\epsilon = 10$, convergence criterion $\zeta = 5 \times 10^{-4}$, maximum number of iterations $k_{\max} = 200$

Input: Cost matrix \mathbf{C} , Normalised concentration vectors $\hat{\mathbf{x}}_A$ and $\hat{\mathbf{x}}_B$

```

1:  $\mathbf{f} \leftarrow \mathbf{0}$ 
2:  $\mathbf{g} \leftarrow \mathbf{0}$ 
3:  $\epsilon \leftarrow \epsilon_0$  ▷ Initialise  $\epsilon$ 
4: while  $\epsilon \geq \epsilon_*$  do
5:    $k \leftarrow 0$  ▷ Number of iterations
6:    $w \leftarrow 10^5$  ▷ Initialise  $w$ 
7:   repeat
8:      $w^- \leftarrow w$  ▷ Previous value of  $w$ 
9:     for  $i = 1$  to  $N$  do
10:       $f_i \leftarrow -\epsilon \ln \left[ \sum_{j=1}^N \exp \left\{ \frac{f_i^{(l)} + g_j^{(l)} - C_{i,j}}{\epsilon} \right\} \right] + f_i^{(l)} + \epsilon \ln \hat{x}_{A,i}$ 
11:     end for
12:     for  $j = 1$  to  $N$  do
13:       $g_j \leftarrow -\epsilon \ln \left[ \sum_{i=1}^N \exp \left\{ \frac{f_i^{(l+1)} + g_j^{(l)} - C_{i,j}}{\epsilon} \right\} \right] + g_j^{(l)} + \epsilon \ln \hat{x}_{B,j}$ 
14:     end for
15:      $\mathbf{P} \leftarrow \exp \left\{ \frac{\mathbf{f}\mathbf{1}^\top + \mathbf{1}\mathbf{g}^\top - \mathbf{C}}{\epsilon} \right\}$ 
16:      $w \leftarrow \sqrt{\sum_{i,j=1}^N C_{i,j} P_{i,j}}$  ▷ Current value of  $w$ 
17:      $k \leftarrow k + 1$ 
18:     until  $|w^- - w|/w < \zeta$  or  $k \geq k_{\max}$  ▷ Convergence criterion
19:      $\epsilon \leftarrow \epsilon/\delta\epsilon$  ▷ Progressively decrease  $\epsilon$ 
20: end while
21: return Wasserstein distance  $w$ 

```

with Σ_A and Σ_B given by

$$\Sigma_A = \mathbf{R}(\theta_A) \Delta_A \mathbf{R}(\theta_A)^\top, \quad (23a)$$

$$\Sigma_B = \mathbf{R}(\theta_B) \Delta_B \mathbf{R}(\theta_B)^\top. \quad (23b)$$

270 In this case, the squared Wasserstein distance between X_A and X_B is given by³

$$w^2(X_A, X_B) = \|\boldsymbol{\mu}_A - \boldsymbol{\mu}_B\|^2 + \text{Tr}(\Sigma_A + \Sigma_B) - 2 \text{Tr} \left(\left[\Sigma_A^{1/2} \Sigma_B \Sigma_A^{1/2} \right]^{\frac{1}{2}} \right). \quad (24)$$

Following the approach of section 2.4, let us now apply the plane transformation \mathbf{F} given by eq. (5) to X_B . The squared Wasserstein distance becomes

$$w^2(X_A, X_B \circ \mathbf{F}) = \|\boldsymbol{\mu}_A - \boldsymbol{\mu}_B + \mathbf{x}_t\|^2 + \text{Tr}(\Delta_A + \Delta_B) - 2 \text{Tr} \left[\Delta_A^{1/2} \mathbf{R}(\theta + \theta_B - \theta_A) \Delta_B \mathbf{R}^\top(\theta + \theta_B - \theta_A) \Delta_A^{1/2} \right]^{\frac{1}{2}}, \quad (25)$$

³By construction, X_A and X_B are normalised, in such a way that we do not need to renormalise them to be able to compute the Wasserstein distance.



275 which depends on x_t , y_t , and θ , the three parameters of \mathbf{F} . It can be shown (see appendix C) that $w^2(X_A, X_B \circ \mathbf{F})$ reaches its minimum when $\mathbf{x}_t = \boldsymbol{\mu}_A - \boldsymbol{\mu}_B$ and $\theta = \theta_A - \theta_B$ (modulo π), in which case the distance is given by

$$w(X_A, X_B \circ \mathbf{F}) = \sqrt{\text{Tr}(\boldsymbol{\Delta}_A + \boldsymbol{\Delta}_B) - 2 \text{Tr} \left[(\boldsymbol{\Delta}_A \boldsymbol{\Delta}_B)^{\frac{1}{2}} \right]}, \quad (26a)$$

$$= \sqrt{\text{Tr} \left[\left(\boldsymbol{\Delta}_A^{\frac{1}{2}} - \boldsymbol{\Delta}_B^{\frac{1}{2}} \right)^2 \right]}, \quad (26b)$$

280 which is known as the Hellinger distance between X_A and X_B (Peyré and Cuturi, 2019). By construction, this distance estimates the shape error between X_A and X_B since the translation, the rotation and the scale differences have been removed. In the following, it will be written w_F to point out the similarity between the relationship d/d_F on the one hand and w/w_F on the other hand.

In the case where X_A and X_B are not exactly Gaussian, we can still use the Gaussian puff model as an approximation. In this case, w_F provides an approximation of the shape error.

285 Finally, an issue with both w and w_F is that they are normalised fields and thus they ignore the scale error, i.e. the difference of total mass between the images. As a consequence, these metrics cannot be used as such in an inversion framework. One way to address this issue is to add to w and w_F a term to represent the scale error. Using the discrete formalism, this term could be

$$d_{\text{mass}}^2(\mathbf{x}_A, \mathbf{x}_B) \propto \left[1 - 2 \frac{\sum_{n=1}^N x_{A,n} \sum_{n=1}^N x_{B,n}}{\left(\sum_{n=1}^N x_{A,n} \right)^2 + \left(\sum_{n=1}^N x_{B,n} \right)^2} \right]^2, \quad (27)$$

290 which is convex. The remaining question would then be the relative contribution of w (or w_F) and d_{mass} in the final distance, which is related to the following question: which kind of error (position, mass, etc.) should be penalised more? This kind of question is beyond the scope of the present article, which is why we only use w and w_F as is in our numerical experiments.

4 Comparison of the metric on analytical test cases

In this section, we evaluate and compare the metrics with a database of images built using a set of Gaussian puffs. The database is introduced in section 4.1, the computation of the non-local metrics is validated in section 4.2, and the behaviour of the metrics on this Gaussian puffs database are compared in section 4.3.

4.1 Gaussian puffs database and experimental setup

The database consists of 10^4 pairs of images constructed using Gaussian puffs and then discretised on the domain $\mathbb{E} = [0, 1]^2$ using a finite resolution of 32×32 pixels. Each puff is parametrised by its mean $\boldsymbol{\mu}$ (two scalars) and its covariance matrix $\boldsymbol{\Sigma} = \mathbf{R}(\theta) \boldsymbol{\Delta} \mathbf{R}(\theta)^\top$ (three scalars: θ and both diagonal entries of $\boldsymbol{\Delta}$), which are randomly drawn as follows:

300 1. both components of $\boldsymbol{\mu}$ are uniformly drawn in $[0.15, 0.85]$;



2. θ is uniformly drawn in $[-\pi, \pi]$;
3. σ_1 and then σ_2 , the two non-zero components of Δ are drawn from a half-normal distribution with a standard deviation of 0.33. If needed, σ_1 and σ_2 are then swapped to ensure $\sigma_1 \geq \sigma_2$.

Ideally, the domain \mathbb{E} should cover a large majority of the mass of each puff. In practice, more than 99% of the mass of a Gaussian puff is covered by the $6\sigma_1 \times 6\sigma_2$ rectangle centred on μ and oriented along the principal axes. For this reason, we repeat step 3 of the random draw until this $6\sigma_1 \times 6\sigma_2$ rectangle is included in the domain \mathbb{E} . In addition, the puffs should not be too small, which is why in our case when $6\sigma_1$ and $6\sigma_2$ are both smaller than 9 pixels, it is rejected and entirely re-drawn.

The characteristics of the database are shown in Figure 3. As expected, the distribution of $\|\mu\|$ is close to Gaussian, the distribution of θ is close to uniform, and the distribution of σ_1 and then σ_2 are close to log-normal.

310 4.2 Validation of the implemented Sinkhorn algorithm

For our Gaussian puffs database, there are four different ways to compute the Wasserstein distance:

1. use the analytical formula eq. (24) with the exact values of $\mu_{A,B}$ and $\Sigma_{A,B}$; this approach will be called w_{th} ;
2. use the analytical formula eq. (24) but with $\mu_{A,B}$ and $\Sigma_{A,B}$ being the sample mean and covariance of the 32×32 -pixel images; this approach is closer to what will be practically done for real image plume, extracting information only from the image, and it will be called w_{num} ;
3. use the Network Simplex algorithm (Bonneel et al., 2011) to find the exact solution of the optimal transport problem using the images like w_{num} ; this approach will be called w_{emd} ;
4. apply the log-Sinkhorn iterations using algorithm 1 using the images like w_{num} ; this approach will be called w_ϵ .

We have applied all four methods and the differences are shown in Figure 4. Note that w_{emd} has been computed using the POT library (Flamary et al., 2021).

The fractional bias over all pairs is no more than 5% when we compare w_{th} to the other three methods of computing the Wasserstein distance. By contrast, w_{emd} and w_{num} are very close to each other. We have checked that the latter phenomenon is reduced when the resolution is increased. Therefore, we conclude that the gap between w_{th} on the one hand, and w_{num} , w_{emd} , and w_ϵ on the other hand is not due to the estimation of the Wasserstein distance but results from the discretisation of the problem with the 32×32 resolution (sampling errors). Figure 4 also shows that w_ϵ matches well w_{emd} , which validates our log-Sinkhorn implementation.

4.3 Correlation to the different error categories

In this subsection, we compare the behaviour of the metrics with respect to three error categories: the translation error, the orientation error, and the shape error. Note that the behaviour with respect to the scale error cannot be compared since the w and w_F distances use normalised images. We used the Pearson correlation as our main indicator of the strength of the link

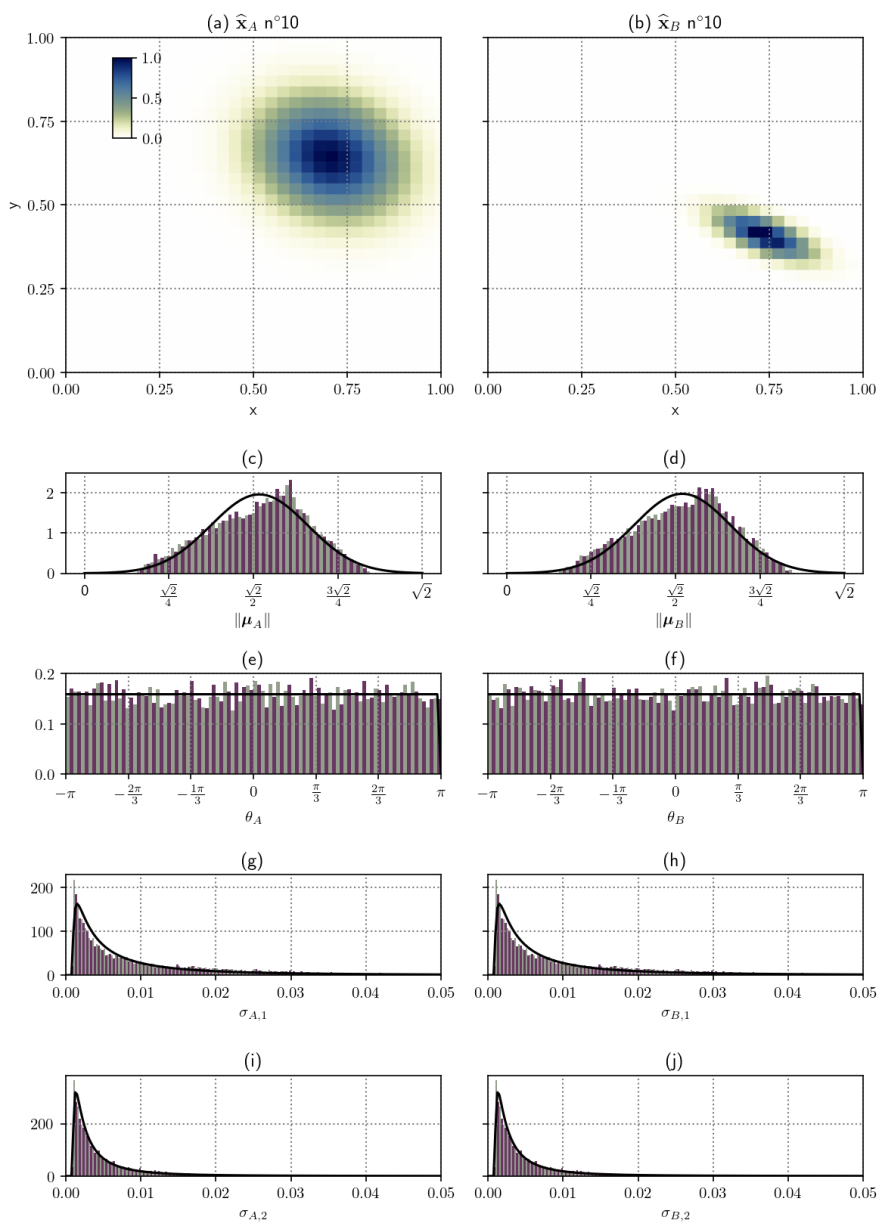


Figure 3. Characteristics of the Gaussian puffs database. (a, b) Images *A* (left) and *B* (right) number 10. (c–j) Histograms of $\|\mu_A\|$ (c), $\|\mu_B\|$ (d), θ_A (e), θ_B (f), $\sigma_{A,1}$ (g), $\sigma_{B,1}$ (h), $\sigma_{A,2}$ (i), and $\sigma_{B,2}$ (j).

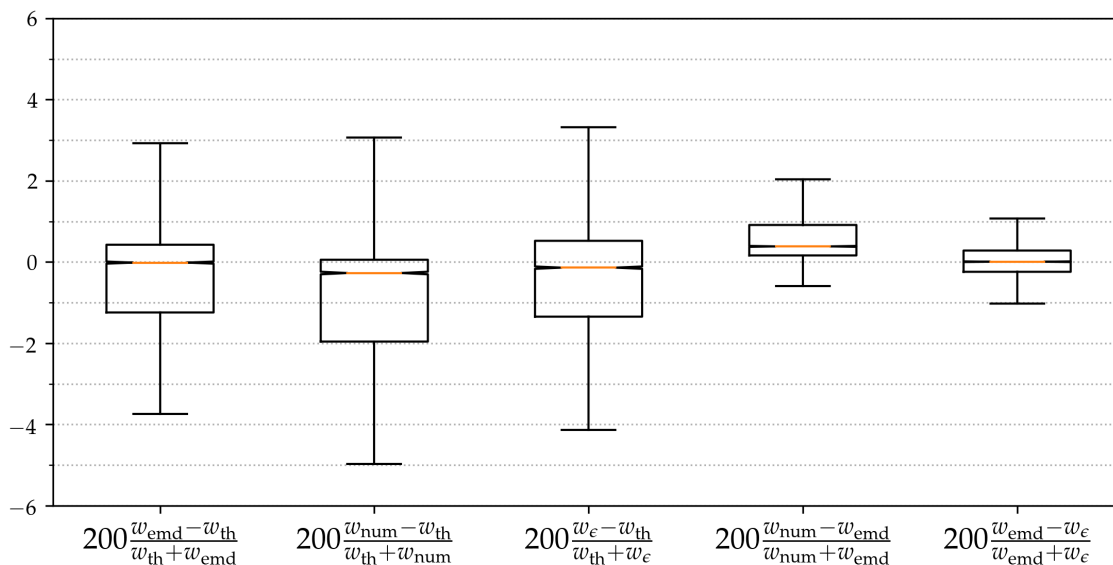


Figure 4. Comparison of the different ways to compute the Wasserstein distance over the Gaussian puffs database. Relative errors between w_{emd} , w_{th} , w_{num} , and w_{ϵ} (c).

Table 2. Correlations between the distances d , w , d_F , and w_F on the one hand, and the quantities T , θ , and H on the other hand for the 10^4 cases in the Gaussian puffs database.

	Pearson correlation		
	T	θ	H
d	0.33	0.00	-0.11
w	0.97	0.00	-0.03
d_F	0.04	-0.01	0.58
w_F	-0.04	-0.01	0.65

between the behaviour of the metrics and the error category. The closer the norm of the Pearson correlation is to one, the more linearly the relation between the quantities is. If the Pearson correlation is positive, then the increase in an error category leads to an increase in the metric value, if negative it leads to a decrease, and if nearly null it means that the two quantities seem independent.

335 For each pair of images in the database, we define T (for *translation*) as $\|\mu_B - \mu_A\|^2$. This quantity represents the translation error between both images. The correlation between T and the four distances is reported in the first column of Table 2.

As expected, the Wasserstein distance w is strongly correlated to T . The \mathcal{L}_2 norm d is also showing a significant correlation of 0.33 to T , highlighting a likely dependency. Both d_F and w_F are designed to be released from the position error and, in



particular, the translation error. This property is confirmed by the very low correlation between T on the one hand and d_F and
340 w_F on the other hand. Additionally, the fact that T is much more correlated to d than to d_F confirms that d indeed depends on
the T quantity.

For each pair of images in the database, we define θ as $\|\theta_B - \theta_A\|$. This quantity represents the orientation error between
both images. The correlation between θ and the four distances is reported in the second column of Table 2. The results shows
also that there is no correlation between θ and any of the distances. In a sense, this shows that all the distances are, for our
345 database, not sensitive to the orientation error.

For each pair of images in the database, we define H as the Hellinger distance between A and B , as given by eq. (26). This is
actually very similar to w_F , but with one exception: H uses the *theoretical* values of Δ_A and Δ_B (i.e. the ones that have been
drawn) while w_F uses the sample covariance of the 32×32 -pixel images. This quantity represents the shape error between
both images. The correlation between H and the four distances is reported in the third column of Table 2.

350 Both d and w show a low correlation to H , which is not the case of d_F and w_F . On the one hand, the correlation between w_F
and H was highly expected from the definition of H . The remaining difference is due to the finite resolution of the images. On
the other hand, the proportionality of d_F with the H was wanted but not assessed. By superimposing optimally the plumes, we
removed the position error but d_F remains sensitive to H , meaning we did not remove all errors. Thus such behaviour reflects
our way of splitting the error. More generally, this comparison on the Gaussian puffs database confirms that both d_F and w_F
355 are freed from the position error and seem to be driven by the shape error.

5 Comparison of the metric on realistic test cases

To go deeper in our analysis, we now compare the metrics using realistic plumes. This section follows the same organisation as
section 4: we present the experimental setup in section 5.1, we validate the computation of the non-local metrics in section 5.2,
and we compare the behaviour of the metrics on this specific database in section 5.3.

360 5.1 Simulation database and experimental setup

We use a simulation database of hourly 3D fields of CO_2 concentrations due to anthropogenic CO_2 emissions from the Neurath
lignite-fired power plant (Germany, 51.04°N , 6.60°E). This database is composed of 14 days of 1h-emission pulses, from July
1 to 14, 2015, i.e. 336 plume transports. Plume transport occurs over fixed 24-hour windows. (from 00:00 to 24:00). Conse-
quently, the later in the day the plumes are emitted the shorter they are tracked. The database is extracted from a larger one,
365 over Western Europe, as described in Potier et al. (2022). Simulations were performed with the CHIMERE Eulerian transport
model (Menut et al., 2013) driven by the Community Inversion Framework (CIF, Berchet et al., 2021). The horizontal grid
resolution of the simulation domain (longitude: 6.82°W to 19.18°N ; latitude: 42.0°N to 56.39°N , Fig. 5, Santaren et al., 2021)
varies between 50km and km. The Neurath power plant is located in the $2\text{km} \times 2\text{km}$ -resolution zoom (longitude: 1.25°W
to 10.64°E ; latitude: 47.45°N to 53.15°N). The vertical grid is composed of 29 pressure layers extending from the surface
370 to 300hPa (approximately 9km above the ground level). CHIMERE is forced by meteorological variables at 9km resolution

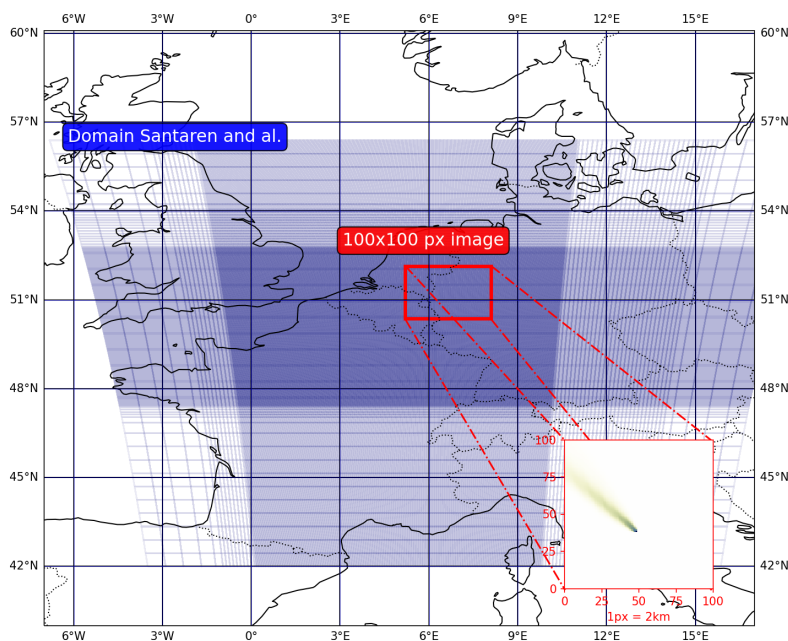


Figure 5. Experimental setup. Simulation domain in blue. Example of an CO₂ image used in red.

(Agusti-Panareda, 2018), provided by the European Centre for Medium-Range Weather Forecasts (ECMWF) for the CO₂ Human Emissions project (CHE, <https://www.che-project.eu/>). The CO₂ emissions from the Neurath power plant are extracted from the ~ 1 km ($1/60^\circ \times 1/120^\circ$) resolution inventory (TNO_GHGco_1x1km_v1_1) of the annual emissions produced by the Netherlands Organisation for Applied Scientific Research (TNO) over Europe for the year 2015 (Denier van der Gon et al., 2017; Super et al., 2020). The temporal disaggregation at the hourly scale is based on coefficients provided with the TNO inventories for the sector A-Public Power, in the Gridded Nomenclature For Reporting (GNFR) of the United Nations Framework Convention on Climate Change (UNFCCC). Emissions are projected on the CHIMERE vertical grid with coefficients corresponding to this A GNFR sector (Bieser et al., 2011), also provided with the TNO inventories.

We ensure that the same daily profile is applied to the source emission, then for a given hour of the day, the difference between two simulated plumes is the meteorological state. We build a database that regroups per pair two simulated plumes at a given hour but from different days (example: day 1 hour 10 versus day 3 hour 10). To get a realistic two-dimensional concentration field, we compute the vertical mean of the concentration weighted by the width of the vertical levels. We ignore the first two hours of the simulation, to ensure that a plume appears in the image. This leaves 2,093 pairs of distinct plumes. The images are cropped to 100x100 pixels (here 1 pixel is equal to 2 km square cell of the simulation) images to reduce the computer resource requirements.

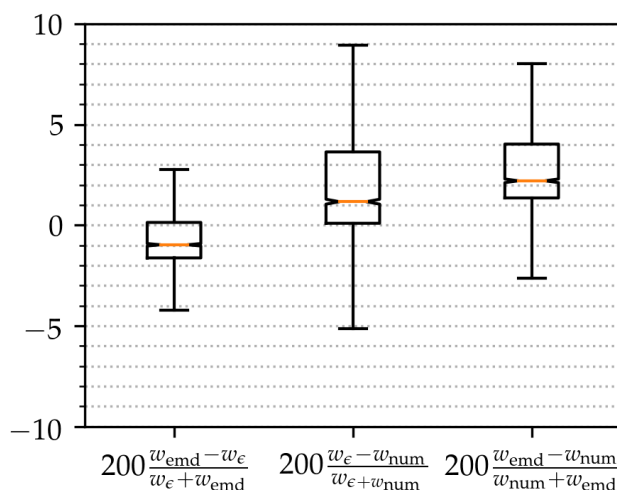


Figure 6. Comparison of the different ways to compute the Wasserstein distance over the realistic database. Relative errors between w_{emd} , w_{num} , and w_{ϵ} (c).

5.2 Comparison of the different estimations of the Wasserstein distance

We have applied all three methods and the differences are shown in Figure 6. The results show, as for the Gaussian puffs database, that w_{ϵ} and w_{emd} are close to each other, which once again validates our algorithm. Moreover, the results show that w_{num} is a reasonably good approximation of w as well. The distance w_{num} makes the approximation that the images are Gaussian puffs, which is a strong approximation but allows for very quick computation. The values of w_{num} seem to be usually lower than those of w_{ϵ} . This previous remark is in agreement with Theorem 2.1 from Gelbrich (1990). It is shown that, for elliptic contour distributions with given mean and covariance matrices, the distance between the two Gaussians with these respective parameters (i.e. w_{num}) is a lower bound of the Wasserstein distance between the two distributions. We are not assured to work with plumes that are elliptic distributions. However, it seems to be a good direction to look at to explain and quantify, if possible, this negative bias. The understanding of the discrepancies between w_{num} and w_{ϵ} is needed to be able to substitute w_{num} to w_{ϵ} , which is why we do not considered thereafter w_{num} in our comparisons.

5.3 Correlation to the different error categories

In this subsection, we compare the behaviour of the metrics with respect to the same three error categories than in section 4.3: the translation, orientation, and shape error. To do so, we keep the same quantities T , θ , and H , with the notable exception that H is now equal to w_F because there is no *theoretical* covariance. The results are reported in Table 3.

While the correlation between w and T remains very strong, d shows less correlation to T than for the Gaussian puffs database. Both d_F and w_F are less correlated to T than d and w , respectively, but their correlation to T is here higher than with



Table 3. Correlations between the distances d , w , d_F , and w_F on the one hand, and the quantities T , θ , and H on the other hand for the 2,093 cases in the realistic database.

	Pearson correlation		
	T	θ	H
d	0.19	-0.04	0.32
w	0.99	0.20	0.37
d_F	0.12	-0.11	0.41
w_F	0.31	0.03	1.00

the Gaussian puffs database. Hence for this realistic database, both d_F and w_F are only partially freed from the translation error.

405 In this case, the correlations between the metrics and θ are higher than for the Gaussian puffs database but again do not prompt a clear conclusion.

By construction, w_F is equal to H , which yields a correlation of 1. Both d and w show a small correlation to H , which was not the case in the Gaussian puffs database. The correlation to H is still higher for d_F , which was expected since d_F is designed to be partially freed from the position error. This result, however, should be taken with caution because here, contrary
410 to the Gaussian puffs database, H now only partially accounts for the shape error between two plumes.

This second study with realistic cases shows that the behaviour of each metric slightly differs from what has been seen in the Gaussian case. Nevertheless, the results confirm that both d_F and w_F are partially freed from the position error while being still sensitive to the shape error, which is what we hoped for.

6 Sensitivity to the meteorological conditions

415 As stated in the introduction, the goal of this article is to develop and test metrics that can discriminate errors stemming from imperfect meteorology from other sources of discrepancies. Therefore, following the approach used in the previous sections, we define here four indicators that we consider representative of the difference in meteorological conditions between the two images. We then examine the correlation between these indicators, the previous indicators (T , θ , and H), and the metrics in the case of the realistic database.

420 6.1 Definition of meteorological indicators

To simplify the analysis, we define four scalar indicators that characterise the meteorological conditions. These indicators focus on the direction and the norm of the wind as experienced by the pollutant during its transportation. For each image, we proceed as follows.



Table 4. Correlations between ΔE_N , ΔE_D , ΔS_N , and ΔS_D on the one hand and T , θ , and H on the other hand for the 2,093 cases in the realistic database.

	Pearson correlation		
	T	θ	H
ΔE_N	0.39	0.23	0.15
ΔE_D	0.52	-0.02	0.30
ΔS_N	0.09	0.04	0.09
ΔS_D	0.06	0.03	0.48

- 425 We first average the wind components (three-dimensional fields) in the vertical direction between the surface and the planetary boundary layer (PBL) height. Indeed, the realistic database has been simulated with summer conditions and hence the plumes are assumed to be dispersed within the PBL. This results in two-dimensional fields for each time snapshot.
2. We compute the norm and the direction of the averaged winds. This results in two two-dimensional fields for each time snapshot.
- 430 3. We average the norm and the direction over the 100×100 -pixel grid. This results in two scalars for each time snapshot.
4. We finally compute the time average and time standard deviation of the averaged norm and direction between midnight (the time at which the emissions started) and the time of the image. This results in four scalars: E_N (averaged wind norm), E_D (averaged wind direction), S_N (deviation of wind norm) and S_D (deviation of wind direction).

The meteorological indicators are then defined as the absolute differences in E_N , E_D , S_N , and S_D between the two images
435 that are compared, simply written ΔE_N , ΔE_D , ΔS_N , and ΔS_D .

6.2 Correlation between the meteorological indicators and the error categories

Using the realistic database, we compute the correlation between ΔE_N , ΔE_D , ΔS_N , and ΔS_D on the one hand and T , θ , and H on the other hand. The idea is to see how differences in the meteorological conditions impact the position and amplitude errors. The results are reported in Table 4.

440 One can notice that T is mainly correlated to ΔE_D and a little less to ΔE_N , while ΔS_D and ΔE_D are correlated to H . This means that differences in meteorology like ΔE_D will likely induce both position error and shape error. Therefore, by removing the position error, we only partially remove the meteorological impact on the differences. Explaining why ΔS_D induces differences in shape is straightforward, but explaining how ΔE_D induces differences in terms of translation instead of orientation is not as so. A difference in the main direction of the plume (which translates into ΔE_D) will move further away
445 the centres of mass from each other, and hence induce a larger T (which is the distance between the two centres of mass). It should be noted that a wind direction change that will keep superimposed the centre of mass will drive orientation error.



Table 5. Correlations between ΔE_N , ΔE_D , ΔS_N , and ΔS_D on the one hand and the distances d , w , d_F , w_F , d^* and d_F^* on the other hand for the 2,093 cases in the realistic database.

	Pearson correlation					
	d	w	d_F	w_F	d^*	d_F^*
ΔE_N	-0.09	0.41	-0.11	0.15	0.07	0.02
ΔE_D	0.14	0.53	0.14	0.30	0.24	0.20
ΔS_N	-0.03	0.11	0.00	0.09	-0.21	-0.17
ΔS_D	0.21	0.09	0.26	0.48	-0.03	0.19

6.3 Correlation between the meteorological indicators and the metrics

To conclude our study, we now compare the different metrics to the meteorological indicators. The results are reported in Table 5.

450 According to the correlations shown in Table 5, the metric w is correlated to ΔE_D and ΔE_N indicators. It is expected since these meteorological changes tend to move the centre of mass and thus increase the translation error. The results show also that w_F sees a drop in correlation to ΔE_D compared to w while getting a correlation with respect to ΔS_D . For optimal transport metrics, we can see that removing the position error does not always remove the sensitivity to a change in meteorology. It should be noticed that increasing in either d or d_F does not seem to be more correlated to our different meteorology indicators.

455 Such lack of correlation compared to the optimal transport theory metrics could result from the weight of the scale error in the distance definition. We normalised the plume the same way as we do for w before computing the distance d and d_F leading us to the normalised image distances d^* and d_F^* . First, d^* and d_F^* are more correlated than d and d_F to ΔE_D and ΔS_N , showing that the scale error is masking the sensitivity of pixel-wise metrics with respect to meteorology. Second, d_F^* gains significantly in correlation to ΔS_D compare to d^* , but remains as correlated to ΔE_D as d^* . Then the plane transformation

460 applied in d_F^* allows a better alignment of the compared plumes, giving more weight to shape error induced by ΔS_D , but does not compensate for all the changes resulting from ΔE_D or ΔE_N .

The lack of correlation to our meteorological indicators for d and d_F seems appealing, but it is due to amplitude error held by a small number of highly concentrated pixels above the source for our cases (i.e. a hot spot). For similar cases, d remains a good metric for updating the inventories. If the "hot spots" of the two images have amplitudes close to each other or there is no

465 "hot-spot" but a large plume, d and d_F become more correlated to several meteorological changes making them less suitable. Pixel-wise metrics seem to be better adapted to compare "hot-spot" and not highly extended plumes. A more versatile metric will be a weighted distance using the w_F , or at least a normalised d_F^* , which is not sensitive to all changes in meteorology, and a term that represents the scale error between the two images.



7 Conclusions

470 In this article, we discussed the use of new metrics for comparing passive gases plumes, practically CO₂ plumes, within an inverse framework aiming at the monitoring of pollutant emissions.

At first, we emphasised how critical the double penalty issue related to pixel-wise comparison is. The traditional \mathcal{L}_2 norm tends to overweight position errors mixing up with other sources of errors. In the context of source inversion, this results in an over-penalised comparison of concentration fields that are slightly shifted from each other, and the mixing makes it difficult to
475 evaluate the relative weight of different types of error afterwards. Yet, for us, the identification of the relative weight of the errors is critical since we want to level down the one due to meteorology and level up the one related to emissions. Assuming that most of the position error is driven by meteorology, we proposed to design metrics that are freed from position error. Following this goal, a pixel-wise metric with an upstream position correction was designed. This new metric has the advantage to keep the formalism of the \mathcal{L}_2 norm while being released from position errors. In addition, it is proposed to use a metric based on
480 the optimal transport theory: the Wasserstein distance. Focusing on the algorithmic aspects related to two-dimensional satellite images, we derived and validated a method to compute this metric. The Wasserstein metric is more sensitive to position errors but it is not hampered by the double penalty issue. To complete our catalogue of metrics, an optimal transport metric freed from position errors is proposed. It can be easily computed with a Gaussian approximation. This metric coincides with the Hellinger distance. Nevertheless, both optimal transport metrics rely on normalised images and thus are unaware of the difference in
485 total mass present in the plumes. The scale factor between the images is linearly related to emission fluxes which we want to estimate. This means that, within the inversion framework, the scale factor between the two images should be added and weighted independently.

These four metrics were compared on a specifically designed Gaussian puffs database and evaluated according to their correlations with respect to translation error, orientation error and shape error. The numerical experiments showed that the
490 resolution of the images tends to impact the optimal transport problem. As expected, the two metrics designed to be freed from position errors are not correlated to translation and orientation errors. The \mathcal{L}_2 norm and Wasserstein metrics are both correlated to the translation error. From this, we extended our tests to a realistic plume database. This second test series shows that, for a more complex plume geometry, the metrics are still correlated to the translation error. This implies that the new metrics are only partially freed from position errors.

495 Then we discussed the link between a position error and a variation within the mesoscale meteorology using the same realistic database. Designing relevant scalar indicators related to meteorological variance, we evaluated how specific changes in meteorological conditions lead to an increase in the distance between the plumes. We have seen that the meteorological changes can be correlated to position errors as well as amplitude errors between plumes. This means that removing the position error from the metrics will not make the comparison insensitive to a meteorological change. However, some metrics were
500 found to be more sensitive to specific changes in the meteorological conditions. For instance, while the Wasserstein metric is sensitive to changes in the main direction or intensity of the winds, the Hellinger metric is more sensitive to changes in the spread of the wind direction both in time and space. This provides guidelines to enlighten the choice of a metric for a given



meteorological situation. By composing with these new metrics freed from position error and additional scaling terms, we get more manageable metrics that will level down in the weight of modelling error due to the meteorology used in the comparison.

505 These metrics are used to quantify the proximity of a couple of plumes and could hence be used in an inverse framework, in particular for processing XCO₂ images. The question of the impact of the meteorological changes on the metrics discussed here can be translated into another question: what importance do we give to each error category? We know that meteorological changes can result in position errors, and we strongly suspect that changes in the emission's temporal profile or vertical distribution can also yield position errors. In such a case, it would be interesting to evaluate the impact of the removal of the

510 position errors and if the amplitude errors carry enough information to compensate. We have seen that amplitude errors can also emerge from changes in meteorology. Thus further studies have to be undergone to evaluate the sensitivity of the metrics to either the emissions or the meteorology, to determine which error has to be more weighted from the perspective of monitoring the emissions. We have to make sure that by removing some sensitivity with respect to meteorology, we are not levelling down by the same factor the sensitivity with respect to the emissions.

515 For an operational purpose, optimising on non-local metrics is much more difficult than on pixel-wise metrics because it requires the computation of non-trivial gradients. The three non-local metrics that we proposed are parameterised. These parameters usually balance a trade-off between computational efficiency and accuracy. For the case of the pixel-wise distance with an upstream correction, this can have an impact on the optimum. Even though this study could be done with a personal computer, further computation optimisation developments are needed for operational use. Here we are only considering passive

520 tracer, but an extension of the study should be using these metrics for reactive pollutants. However, it requires quantifying the relative impact of chemistry on the shape, the scale and the position of the plume.

The key idea here is that meteorology is fixed and bounds our model predictions. We choose to develop metrics that aim to remove the weight of such bound within the comparison to the observation. We could instead consider that meteorology is not fixed and can be seen as additional degrees of freedom to estimate. Thus the Wasserstein metric is interesting due to its softer

525 behaviour than pixel-wise metrics but remains numerically costly. Yet, we have seen that approximating the plume by Gaussian puffs yields a cheap estimate of the true Wasserstein distance. To ease the computation, we suggest using an approximation of the Wasserstein distance, assuming Gaussian puff-like plumes or separable into a Gaussian mixture as in Chen et al. (2019); Delon and Desolneux (2020). But the relevance of these approximations has to be discussed when it comes to real, noisy, cloudy, plume images. This paper was a first step towards the use of smarter metrics to compare plume images to monitor

530 atmospheric gaseous compound emissions through an inverse method.

Data availability. All the data required to get the presented results are available on the zenodo deposit (Vanderbecken, 2022)



Appendix A: Notation

Notations	
\mathbf{x}	Position vector in the image
$X_{A,B}$	Continuous interpolation of the concentration field
$\mathbf{x}_{A,B}$	Discrete representation of the concentration field
$\hat{\mathbf{x}}_{A,B}$	Normalised discrete concentration field
$\mathcal{N}(\boldsymbol{\mu}, \boldsymbol{\Sigma})$	Normal distribution of mean $\boldsymbol{\mu}$ and error covariance matrix $\boldsymbol{\Sigma}$
$\mathcal{U}_{\mathbb{E}}$	Uniform distribution over the domain \mathbb{E}
$\boldsymbol{\mu}$	Always refers to a mean vector
$\boldsymbol{\Sigma}$	Always refers to an error covariance matrix
$\boldsymbol{\Delta}$	Diagonal matrix with the eigenvalues of $\boldsymbol{\Sigma}$
$\mathbf{R}(\theta)$	Rotation matrix of angle θ
\mathbf{x}_t	Translation vector
\mathbf{x}_0	Centre of mass coordinate vector
\mathbf{F}	Transformation in the plane
d	Usual pixel-wise Euclidean distance
d_F	Pixel-wise distance with an upstream position correction
w	Wasserstein distance
w_F	Wasserstein distance with an upstream position correction
w_{emd}	Earth mover distance
w_{ϵ}	Log-Sinkhorn approximation of the Wasserstein distance
w_{num}	Wasserstein distance between two Gaussian puffs
w_{th}	Analytical Wasserstein distance between two Gaussian puffs
ϵ	Weight of the entropic regularisation of the log-Sinkhorn algorithm
ζ	Convergence criterion for the log-Sinkhorn algorithm
T	Translation length between the centre of mass of two plumes
θ	Rotation angle between the principal axes of two plumes
H	Hellinger distance between the error covariance matrices of two plumes
E_N	Mean wind speed seen by the plume averaged over the image domain and time
E_D	Mean wind direction seen by the plume averaged over the image domain and time
S_N	Standard deviation of the wind speed seen by the plume across the image domain and time
S_D	Standard deviation of the wind direction seen by the plume across the image domain and time



Appendix B: Gradient of the cost function for d_F

To minimise eq. (8) we use the L-BFGS algorithm provided by the SciPy library. The algorithm explicitly uses the gradient of the cost function \mathcal{J} with respect to θ , x_t , and y_t . The first term of this gradient – corresponding to $d^2(X_A, X_B \circ \mathbf{F})$ – is given by

$$\frac{\partial \mathcal{J}}{\partial \alpha} = -2 \int_{\mathbb{R}^2} [X_A(\mathbf{x}) - X_A(\mathbf{F}(\mathbf{x}))] \left[\frac{\partial X_B}{\partial x}(\mathbf{F}(\mathbf{x})) \cdot \frac{\partial F_x}{\partial \alpha} + \frac{\partial X_B}{\partial y}(\mathbf{F}(\mathbf{x})) \cdot \frac{\partial F_y}{\partial \alpha} \right] d\mathbf{x}, \quad (\text{B1})$$

where α is either θ , x_t , or y_t , $\mathbf{x} = (x, y)^\top$, and $\mathbf{F} = (F_x, F_y)^\top$. The partial derivatives of X_B are given by the second image (using the interpolation method), and the partial derivative of F_x and F_y are

$$540 \quad \frac{\partial F_x}{\partial \theta} = -(x - x_0) \sin \theta - (y - y_0) \cos \theta, \quad \frac{\partial F_y}{\partial \theta} = (x - x_0) \cos \theta - (y - y_0) \sin \theta, \quad (\text{B2a})$$

$$\frac{\partial F_x}{\partial x_t} = 1, \quad \frac{\partial F_y}{\partial x_t} = 0, \quad (\text{B2b})$$

$$\frac{\partial F_x}{\partial y_t} = 0, \quad \frac{\partial F_y}{\partial y_t} = 1. \quad (\text{B2c})$$

Appendix C: From the Wasserstein distance w to the Hellinger distance w_F

Let us define the cost function

$$545 \quad \mathcal{J}(x_t, y_t, \theta) \triangleq w^2(X_A, X_B \circ \mathbf{F}), \quad (\text{C1})$$

where $w^2(X_A, X_B \circ \mathbf{F})$ is given by eq. (25). The goal is to minimise \mathcal{J} . From eq. (25), we remark that \mathcal{J} has three terms $\mathcal{J} = \mathcal{J}_1 + \mathcal{J}_2 + \mathcal{J}_3$, with

$$\mathcal{J}_1 \triangleq \text{Tr}(\mathbf{\Delta}_A + \mathbf{\Delta}_B), \quad (\text{C2})$$

$$\mathcal{J}_2(x_t, y_t) \triangleq \|\boldsymbol{\mu}_A - \boldsymbol{\mu}_B + \mathbf{x}_t\|^2, \quad (\text{C3})$$

$$550 \quad \mathcal{J}_3(\theta) \triangleq -2 \text{Tr} \left[\mathbf{\Delta}_A^{1/2} \mathbf{R}(\theta + \theta_B - \theta_A) \mathbf{\Delta}_B \mathbf{R}(\theta + \theta_B - \theta_A)^\top \mathbf{\Delta}_A^{1/2} \right]^{\frac{1}{2}}. \quad (\text{C4})$$

Minimising \mathcal{J} with respect to (x_t, y_t, θ) is equivalent to minimising \mathcal{J}_2 with respect to (x_t, y_t) and minimising \mathcal{J}_3 with respect to θ . The minimum of \mathcal{J}_2 is 0 and is reached for $\mathbf{x}_t = \boldsymbol{\mu}_B - \boldsymbol{\mu}_A$. Let us now focus on the minimum of \mathcal{J}_3 . For convenience, we define

$$\mathbf{M}(\theta) \triangleq \mathbf{\Delta}_A^{1/2} \mathbf{R}(\theta + \theta_B - \theta_A) \mathbf{\Delta}_B \mathbf{R}(\theta + \theta_B - \theta_A)^\top \mathbf{\Delta}_A^{1/2}, \quad (\text{C5})$$



555 in such a way that $\mathcal{J}_3(\theta) = -2 \text{Tr} \mathbf{M}(\theta)^{\frac{1}{2}}$. With our notation, we have

$$\mathbf{\Delta}_A = \begin{bmatrix} \sigma_{1,A} & 0 \\ 0 & \sigma_{2,A} \end{bmatrix}, \quad (\text{C6a})$$

$$\mathbf{\Delta}_B = \begin{bmatrix} \sigma_{1,B} & 0 \\ 0 & \sigma_{2,B} \end{bmatrix}, \quad (\text{C6b})$$

$$\mathbf{R}(\theta + \theta_B - \theta_A) = \begin{bmatrix} \cos \tilde{\theta} & -\sin \tilde{\theta} \\ \sin \tilde{\theta} & \cos \tilde{\theta} \end{bmatrix}, \quad (\text{C6c})$$

where $\tilde{\theta} \triangleq \theta + \theta_B - \theta_A$, and hence

$$560 \quad \mathbf{M}(\theta) = \begin{bmatrix} \sigma_{1,A}\sigma_{1,B} \cos^2 \tilde{\theta} + \sigma_{1,A}\sigma_{2,B} \sin^2 \tilde{\theta} & \sqrt{\sigma_{1,A}\sigma_{2,A}}(\sigma_{1,B} - \sigma_{2,B}) \cos \tilde{\theta} \sin \tilde{\theta} \\ \sqrt{\sigma_{1,A}\sigma_{2,A}}(\sigma_{1,B} - \sigma_{2,B}) \cos \tilde{\theta} \sin \tilde{\theta} & \sigma_{2,A}\sigma_{2,B} \cos^2 \tilde{\theta} + \sigma_{2,A}\sigma_{1,B} \sin^2 \tilde{\theta} \end{bmatrix}. \quad (\text{C7})$$

By construction, $\mathbf{M}(\theta)$ is symmetric and positive definite, therefore it is diagonalisable with strictly positive eigenvalues $\lambda_{\pm}(\theta)$. As a consequence, we have

$$\text{Tr} \mathbf{M}(\theta)^{\frac{1}{2}} = \sqrt{\lambda_+(\theta)} + \sqrt{\lambda_-(\theta)}. \quad (\text{C8})$$

Let us now introduce the following ancillary quantities:

$$565 \quad \alpha \triangleq \sigma_{1,A}\sigma_{1,B} + \sigma_{2,A}\sigma_{2,B}, \quad (\text{C9a})$$

$$\beta \triangleq \sigma_{1,A}\sigma_{2,B} + \sigma_{2,A}\sigma_{1,B}, \quad (\text{C9b})$$

$$\kappa(\theta) \triangleq \text{Tr} \mathbf{M}(\theta) = \alpha \cos^2 \tilde{\theta} + \beta \sin^2 \tilde{\theta}, \quad (\text{C9c})$$

$$\gamma(\theta) \triangleq \kappa^2(\theta) - 4 \det \mathbf{M}(\theta) = \kappa^2(\theta) - 4\sigma_{1,A}\sigma_{1,B}\sigma_{2,A}\sigma_{2,B}. \quad (\text{C9d})$$

570 Note that $\gamma(\theta)$ is the discriminant of the characteristic polynomial of $\mathbf{M}(\theta)$, which means that $\gamma(\theta) \geq 0$ because $\mathbf{M}(\theta)$ is symmetric and positive definite. With these quantities, we have

$$\lambda_{\pm}(\theta) = \frac{1}{2} \left(\kappa(\theta) \pm \sqrt{\gamma(\theta)} \right). \quad (\text{C10})$$

Let us first consider the case $\gamma(\theta) = 0$. In this case, $\lambda_+(\theta) = \lambda_-(\theta) \triangleq \lambda(\theta)$, in other words $\mathbf{M}(\theta) = \lambda(\theta) \mathbf{I}$. From the definition of $\mathbf{M}(\theta)$, eq. (C5), we deduce that

$$\mathbf{R}(\tilde{\theta}) \mathbf{\Delta}_B \mathbf{R}(\tilde{\theta})^{\top} = \lambda(\theta) \mathbf{\Delta}_A, \quad (\text{C11})$$

575 which enforces $\tilde{\theta} = 0$ (modulo π). This means that eq. (C7) simplifies into

$$\mathbf{M}(\theta) = \begin{bmatrix} \sigma_{1,A}\sigma_{1,B} & 0 \\ 0 & \sigma_{2,A}\sigma_{2,B} \end{bmatrix}, \quad (\text{C12})$$



and hence $\lambda(\theta) = \sigma_{1,A}\sigma_{1,B} = \sigma_{2,A}\sigma_{2,B}$. Without loss of generality, we can assume in the definition of Δ_A and θ_A that $0 < \sigma_{1,A} \leq \sigma_{2,A}$ and the same for B^4 . This means that $\sigma_{1,A}\sigma_{1,B} = \sigma_{2,A}\sigma_{2,B}$ actually implies $\sigma_{1,A} = \sigma_{2,A}$ and $\sigma_{1,B} = \sigma_{2,B}$. In this case, the covariance matrices for A and B are isotropic and \mathcal{J}_3 does not actually depend on θ .

580 Let us now consider the non-isotropic case: $0 < \sigma_{1,A} < \sigma_{2,A}$ and $0 < \sigma_{1,B} < \sigma_{2,B}$, which is the only case where \mathcal{J}_3 depends on θ . In this case, we necessarily have $\gamma(\theta) > 0$. We can then take the derivative of \mathcal{J}_3 with respect to θ :

$$-\frac{1}{2}\mathcal{J}'_3(\theta) = \frac{\lambda'_+(\theta)}{2\sqrt{\lambda_+(\theta)}} + \frac{\lambda'_-(\theta)}{2\sqrt{\lambda_-(\theta)}}, \quad (\text{C13})$$

$$= \frac{\sqrt{\lambda_+(\theta)}\lambda'_+(\theta)}{2\lambda_+(\theta)} + \frac{\sqrt{\lambda_-(\theta)}\lambda'_-(\theta)}{2\lambda_-(\theta)}, \quad (\text{C14})$$

$$= \frac{\sqrt{\lambda_+(\theta)}\left(\kappa'(\theta) + \frac{\gamma'(\theta)}{2\sqrt{\gamma(\theta)}}\right)}{4\lambda_+(\theta)} + \frac{\sqrt{\lambda_-(\theta)}\left(\kappa'(\theta) - \frac{\gamma'(\theta)}{2\sqrt{\gamma(\theta)}}\right)}{4\lambda_-(\theta)}, \quad (\text{C15})$$

$$585 = \frac{\frac{\sqrt{\lambda_+(\theta)}}{\sqrt{\gamma(\theta)}}\left(\kappa'(\theta)\sqrt{\gamma(\theta)} + \frac{1}{2}\gamma'(\theta)\right)}{4\lambda_+(\theta)} + \frac{\frac{\sqrt{\lambda_-(\theta)}}{\sqrt{\gamma(\theta)}}\left(\kappa'(\theta)\sqrt{\gamma(\theta)} - \frac{1}{2}\gamma'(\theta)\right)}{4\lambda_-(\theta)}, \quad (\text{C16})$$

$$= \frac{\frac{\sqrt{\lambda_+(\theta)}}{\sqrt{\gamma(\theta)}}\left(\kappa'(\theta)\sqrt{\gamma(\theta)} + \kappa'(\theta)\kappa(\theta)\right)}{4\lambda_+(\theta)} + \frac{\frac{\sqrt{\lambda_-(\theta)}}{\sqrt{\gamma(\theta)}}\left(\kappa'(\theta)\sqrt{\gamma(\theta)} - \kappa'(\theta)\kappa(\theta)\right)}{4\lambda_-(\theta)}, \quad (\text{C17})$$

$$= \frac{2\frac{\sqrt{\lambda_+(\theta)}}{\sqrt{\gamma(\theta)}}\kappa'(\theta)\lambda_+(\theta)}{4\lambda_+(\theta)} - \frac{2\frac{\sqrt{\lambda_-(\theta)}}{\sqrt{\gamma(\theta)}}\kappa'(\theta)\lambda_-(\theta)}{4\lambda_-(\theta)}, \quad (\text{C18})$$

$$= \kappa'(\theta) \cdot \frac{\sqrt{\lambda_+(\theta)} - \sqrt{\lambda_-(\theta)}}{2\sqrt{\gamma(\theta)}}, \quad (\text{C19})$$

$$= (\beta - \alpha)\cos\tilde{\theta}\sin\tilde{\theta} \cdot \frac{\sqrt{\lambda_+(\theta)} - \sqrt{\lambda_-(\theta)}}{\sqrt{\gamma(\theta)}}, \quad (\text{C20})$$

590 which is the product of three terms: $\beta - \alpha$, $\cos\tilde{\theta}\sin\tilde{\theta}$, and $\left(\sqrt{\lambda_+(\theta)} - \sqrt{\lambda_-(\theta)}\right)/\sqrt{\gamma(\theta)}$. The third term is always strictly positive because $\gamma(\theta) > 0$. The first term is always strictly negative because we have assumed that $\sigma_{1,A} < \sigma_{2,A}$ and $\sigma_{1,B} < \sigma_{2,B}$. Hence we only need to consider the second term $\cos\tilde{\theta}\sin\tilde{\theta}$ to conclude that the minima of \mathcal{J}_3 are met for $\tilde{\theta} = 0$ (modulo π) or equivalently $\theta = \theta_A - \theta_B$ (modulo π). In this case, $\mathbf{M}(\theta) = \Delta_A\Delta_B$ and $\mathcal{J}_3(\theta) = -2\text{Tr}(\Delta_A\Delta_B)$, which yields the correct formula for w_F , eq. (26). Finally note that this formula is also valid in the case where at least one of A or B is isotropic.

595 *Author contributions.* 1) writing process: mainly PV and EP with inputs from all co-authors, 2) System and experiment design: PV, JD, AF, MB, YR 3) Implementation: PV, 4) support in development and use of data: PV, EP 5) Analysis: mainly PV, JD, AF, MB with feedbacks from all co authors

⁴If this is not the case, we just have to change θ_A into $\theta_A + \pi$ to swap $\sigma_{1,A}$ and $\sigma_{2,A}$.



Competing interests. The authors declare that they have no conflict of interest.

600 *Acknowledgements.* This study has been funded by the national research project ANR-ARGONAUT N° ANR-19-CE01-0007 (Pollutants and greenhouse gases emissions monitoring from space at high resolution). Joffrey Dumont le Brazidec is supported by the European Union's Horizon 2020 research and innovation programme under grant agreement N° 958927 (Prototype system for a Copernicus CO2service). All the figures are drawn using CVD-friendly colormaps. It was made possible using a Python wrapper around Fabio Crameri's perceptually uniform colormaps (Crameri, 2021), available here <https://www.fabiocrameri.ch/colourmaps/>. CEREAs is a member of Institut Pierre-Simon Laplace (IPSL).



605 References

- Agusti-Panareda, A.: The CHE Tier1 Global Nature Run, Tech. rep., CO2 Human Emissions, H2020 European Project, <https://www.che-project.eu/sites/default/files/2018-07/CHE-D2.2-V1-0.pdf>, 2018.
- Amodei, M., Sanchez, I., and Stein, J.: Deterministic and fuzzy verification of the cloudiness of High Resolution operational models, *Meteorological Applications*, 16, 191–203, <https://doi.org/10.1002/met.101>, conference Name: 9th EMS Annual Meeting Pages: EMS2009-587
610 ADS Bibcode: 2009ems..confE.587A, 2009.
- Benamou, J.-D. and Brenier, Y.: A computational fluid mechanics solution to the Monge-Kantorovich mass transfer problem, *Numerische Mathematik*, 84, 375–393, <https://doi.org/10.1007/s002110050002>, 2000.
- Berchet, A., Sollum, E., Thompson, R. L., Pison, I., Thanwerdas, J., Broquet, G., Chevallier, F., Aalto, T., Berchet, A., Bergamaschi, P., Brunner, D., Engelen, R., Fortems-Cheiney, A., Gerbig, C., Groot Zwaaftink, C. D., Haussaire, J.-M., Henne, S., Houweling, S., Karstens,
615 U., Kutsch, W. L., Luijkx, I. T., Monteil, G., Palmer, P. I., van Peet, J. C. A., Peters, W., Peylin, P., Potier, E., Rödenbeck, C., Saunio, M., Scholze, M., Tsuruta, A., and Zhao, Y.: The Community Inversion Framework v1.0: a unified system for atmospheric inversion studies, *Geoscientific Model Development*, 14, 5331–5354, <https://doi.org/10.5194/gmd-14-5331-2021>, 2021.
- Bieser, J., Aulinger, A., Matthias, V., Quante, M., and Denier van der Gon, H.: Vertical emission profiles for Europe based on plume rise calculations, *Environmental Pollution*, 159, 2935–2946, <https://doi.org/10.1016/j.envpol.2011.04.030>, nitrogen Deposition, Critical Loads
620 and Biodiversity, 2011.
- Bonneel, N., van de Panne, M., Paris, S., and Heidrich, W.: Displacement Interpolation Using Lagrangian Mass Transport, in: *Proceedings of the 2011 SIGGRAPH Asia Conference*, SA '11, Association for Computing Machinery, New York, NY, USA, <https://doi.org/10.1145/2024156.2024192>, 2011.
- Briggs, W. M. and Levine, R. A.: Wavelets and Field Forecast Verification, *Monthly Weather Review*, 125, 1329–1341,
625 [https://doi.org/10.1175/1520-0493\(1997\)125<1329:WAFV>2.0.CO;2](https://doi.org/10.1175/1520-0493(1997)125<1329:WAFV>2.0.CO;2), publisher: American Meteorological Society Section: Monthly Weather Review, 1997.
- Broquet, G., Bréon, F.-M., Renault, E., Buchwitz, M., Reuter, M., Bovensmann, H., Chevallier, F., Wu, L., and Ciais, P.: The potential of satellite spectro-imagery for monitoring CO₂ emissions from large cities, *Atmospheric Measurement Techniques*, 11, 681–708, <https://doi.org/10.5194/amt-11-681-2018>, publisher: Copernicus GmbH, 2018.
- 630 Brunner, D., Kuhlmann, G., Marshall, J., Clément, V., Fuhrer, O., Broquet, G., Löscher, A., and Meijer, Y.: Accounting for the vertical distribution of emissions in atmospheric CO₂ simulations, *Atmospheric Chemistry and Physics*, 19, 4541–4559, <https://doi.org/10.5194/acp-19-4541-2019>, publisher: Copernicus GmbH, 2019.
- Cai, B., Cui, C., Zhang, D., Cao, L., Wu, P., Pang, L., Zhang, J., and Dai, C.: China city-level greenhouse gas emissions inventory in 2015 and uncertainty analysis, *Applied Energy*, 253, 113 579, <https://doi.org/https://doi.org/10.1016/j.apenergy.2019.113579>, 2019.
- 635 Calvo Buendia, E., E., Tanabe, K., Kranjc, A., Baasansuren, J., Fukuda, M., Ngarize, S., Osako, A., Pyrozhenko, Y., Shermanau, P., and Frederici, S.: Quality Assurance/ Quality Control and Verification, in: *2019 Refinement to the 2006 IPCC Guidelines for National Greenhouse Gas Inventories*, vol. 1, IPCC, ipcc, switzerland edn., https://www.ipcc-nggip.iges.or.jp/public/2019rf/pdf/1_Volume1/19R_V1_Ch03_Uncertainties.pdf, 2019a.
- 640 Calvo Buendia, E., E., Tanabe, K., Kranjc, A., Baasansuren, J., Fukuda, M., Ngarize, S., Osako, A., Pyrozhenko, Y., Shermanau, P., and Frederici, S.: Uncertainties, in: *2019 Refinement to the 2006 IPCC Guidelines for National Greenhouse Gas Inventories*, vol. 1, IPCC, ipcc, switzerland edn., https://www.ipcc-nggip.iges.or.jp/public/2019rf/pdf/1_Volume1/19R_V1_Ch03_Uncertainties.pdf, 2019b.



- Chen, Y., Georgiou, T. T., and Tannenbaum, A.: Optimal Transport for Gaussian Mixture Models, *IEEE Access*, 7, 6269–6278, <https://doi.org/10.1109/ACCESS.2018.2889838>, conference Name: IEEE Access, 2019.
- Chizat, L., Peyré, G., Schmitzer, B., and Vialard, F.-X.: Scaling algorithms for unbalanced optimal transport problems, *Mathematics of*
645 *Computation*, 87, 2563–2609, <https://doi.org/10.1090/mcom/3303>, 2018.
- Cramer, F.: Scientific colour maps, <https://doi.org/10.5281/zenodo.5501399>, The development of the Scientific colour maps is not funded any longer, but will continue as a pro bono project for the scientific community. - Fabio, 2021.
- Davis, C., Brown, B., and Bullock, R.: Object-Based Verification of Precipitation Forecasts. Part I: Methodology and Application to
650 *Mesoscale Rain Areas*, *Monthly Weather Review*, 134, 1772–1784, <https://doi.org/10.1175/MWR3145.1>, publisher: American Meteorological Society Section: *Monthly Weather Review*, 2006.
- Davis, D. S.: Object-based image analysis: a review of developments and future directions of automated feature detection in landscape archaeology, *Archaeological Prospection*, 26, 155–163, <https://doi.org/10.1002/arp.1730>, _eprint: <https://onlinelibrary.wiley.com/doi/pdf/10.1002/arp.1730>, 2019.
- Delon, J. and Desolneux, A.: A Wasserstein-Type Distance in the Space of Gaussian Mixture Models, *SIAM Journal on Imaging Sciences*,
655 13, 936–970, <https://doi.org/10.1137/19M1301047>, publisher: Society for Industrial and Applied Mathematics, 2020.
- Denier van der Gon, H. A. C., Kuenen, J. J. P., Janssens-Maenhout, G., Döring, U., Jonkers, S., and Visschedijk, A.: TNO_CAMS high resolution European emission inventory 2000-2014 for anthropogenic CO₂ and future years following two different pathways, *Earth System Science Data Discussions*, pp. 1–30, <https://doi.org/10.5194/essd-2017-124>, publisher: Copernicus GmbH, 2017.
- Dumont Le Brazidec, J., Bocquet, M., Saunier, O., and Roustan, Y.: Quantification of uncertainties in the assessment of an atmospheric release
660 source applied to the autumn 2017 ¹⁰⁶Ru event, *Atmospheric Chemistry and Physics*, 21, 13 247–13 267, <https://doi.org/10.5194/acp-21-13247-2021>, 2021.
- Ebert, E. E.: Fuzzy verification of high-resolution gridded forecasts: a review and proposed framework, *Meteorological Applications*, 15, 51–64, <https://doi.org/10.1002/met.25>, _eprint: <https://onlinelibrary.wiley.com/doi/pdf/10.1002/met.25>, 2008.
- Farchi, A., Bocquet, M., Roustan, Y., Mathieu, A., and Quérel, A.: Using the Wasserstein distance to compare fields of pollutants: application
665 to the radionuclide atmospheric dispersion of the Fukushima-Daiichi accident, *Tellus B: Chemical and Physical Meteorology*, 68, 31 682, <https://doi.org/10.3402/tellusb.v68.31682>, publisher: Taylor & Francis _eprint: <https://doi.org/10.3402/tellusb.v68.31682>, 2016.
- Feyeux, N., Vidard, A., and Nodet, M.: Optimal transport for variational data assimilation, *Nonlinear Processes in Geophysics*, 25, 55–66, <https://doi.org/10.5194/npg-25-55-2018>, publisher: Copernicus GmbH, 2018.
- Flamary, R., Courty, N., Gramfort, A., Alaya, M. Z., Boisbunon, A., Chambon, S., Chapel, L., Corenflos, A., Fatras, K., Fournier, N.,
670 Gautheron, L., Gayraud, N. T. H., Janati, H., Rakotomamonjy, A., Redko, I., Rolet, A., Schutz, A., Seguy, V., Sutherland, D. J., Tavenard, R., Tong, A., and Vayer, T.: POT: Python Optimal Transport, *Journal of Machine Learning Research*, 22, 1–8, <http://jmlr.org/papers/v22/20-451.html>, 2021.
- Gelbrich, M.: On a Formula for the L2 Wasserstein Metric between Measures on Euclidean and Hilbert Spaces, *Mathematische Nachrichten*, 147, 185–203, <https://doi.org/10.1002/mana.19901470121>, _eprint: <https://onlinelibrary.wiley.com/doi/pdf/10.1002/mana.19901470121>,
675 1990.
- Gilleland, E.: Novel measures for summarizing high-resolution forecast performance, *Advances in Statistical Climatology, Meteorology and Oceanography*, 7, 13–34, publisher: Copernicus GmbH, 2021.



- Gilleland, E., Ahijevych, D., Brown, B. G., Casati, B., and Ebert, E. E.: Intercomparison of Spatial Forecast Verification Methods, *Weather and Forecasting*, 24, 1416–1430, <https://doi.org/10.1175/2009WAF2222269.1>, publisher: American Meteorological Society Section: 680 *Weather and Forecasting*, 2009.
- Hakkarainen, J., Szelağ, M. E., Ialongo, I., Retscher, C., Oda, T., and Crisp, D.: Analyzing nitrogen oxides to carbon dioxide emission ratios from space: A case study of Matimba Power Station in South Africa, *Atmospheric Environment: X*, 10, 100–110, <https://doi.org/10.1016/j.aeaoa.2021.100110>, 2021.
- Hergoualc’h, K., Mueller, N., Bernoux, M., Kasimir, A., van der Weerden, T. J., and Ogle, S. M.: Improved accuracy and reduced uncertainty 685 in greenhouse gas inventories by refining the IPCC emission factor for direct N₂O emissions from nitrogen inputs to managed soils, *Global Change Biology*, 27, 6536–6550, <https://doi.org/10.1111/gcb.15884>, _eprint: <https://onlinelibrary.wiley.com/doi/pdf/10.1111/gcb.15884>, 2021.
- Hoffman, R. N. and Grassotti, C.: A Technique for Assimilating SSM/I Observations of Marine Atmospheric Storms: Tests with ECMWF Analyses, *Journal of Applied Meteorology and Climatology*, 35, 1177–1188, [https://doi.org/10.1175/1520-0450\(1996\)035<1177:ATFASO>2.0.CO;2](https://doi.org/10.1175/1520-0450(1996)035<1177:ATFASO>2.0.CO;2), publisher: American Meteorological Society Section: *Journal of Applied Meteorology and Climatology*, 1996. 690
- Hoffman, R. N., Liu, Z., Louis, J.-F., and Grassotti, C.: Distortion Representation of Forecast Errors, *Monthly Weather Review*, 123, 2758–2770, [https://doi.org/10.1175/1520-0493\(1995\)123<2758:DROFE>2.0.CO;2](https://doi.org/10.1175/1520-0493(1995)123<2758:DROFE>2.0.CO;2), publisher: American Meteorological Society Section: *Monthly Weather Review*, 1995.
- 695 Horowitz, C. A.: Paris Agreement, *International Legal Materials*, 55, 740–755, <https://doi.org/10.1017/S0020782900004253>, publisher: Cambridge University Press, 2016.
- Janssens-Maenhout, G., Crippa, M., Guizzardi, D., Muntean, M., Schaaf, E., Dentener, F., Bergamaschi, P., Pagliari, V., Olivier, J. G. J., Peters, J. A. H. W., van Aardenne, J. A., Monni, S., Doering, U., Petrescu, A. M. R., Solazzo, E., and Oreggioni, G. D.: EDGAR v4.3.2 Global Atlas of the three major greenhouse gas emissions for the period 1970–2012, *Earth System Science Data*, 11, 959–1002, 700 <https://doi.org/10.5194/essd-11-959-2019>, publisher: Copernicus GmbH, 2019.
- Kantorovich, L. V.: On mass transportation, *C. R. (Doklady) Acad. Sci. URSS (N. S.)*, 37, 199–201, <https://ci.nii.ac.jp/naid/10018386680/>, 1942.
- Keil, C. and Craig, G. C.: A Displacement-Based Error Measure Applied in a Regional Ensemble Forecasting System, *Monthly Weather Review*, 135, 3248–3259, <https://doi.org/10.1175/MWR3457.1>, publisher: American Meteorological Society Section: *Monthly Weather Review*, 2007. 705
- Korsakissok, I. and Mallet, V.: Comparative Study of Gaussian Dispersion Formulas within the Polyphemus Platform: Evaluation with Prairie Grass and Kincaid Experiments, *Journal of Applied Meteorology and Climatology*, 48, 2459–2473, <https://doi.org/10.1175/2009JAMC2160.1>, publisher: American Meteorological Society Section: *Journal of Applied Meteorology and Climatology*, 2009.
- 710 Kuenen, J. J. P., Visschedijk, A. J. H., Jozwicka, M., and Denier van der Gon, H. a. C.: TNO-MACC_II emission inventory; a multi-year (2003–;2009) consistent high-resolution European emission inventory for air quality modelling, *Atmospheric Chemistry and Physics*, 14, 10963–10976, <https://doi.org/10.5194/acp-14-10963-2014>, publisher: Copernicus GmbH, 2014.
- Kuhlmann, G., Broquet, G., Marshall, J., Clément, V., Löscher, A., Meijer, Y., and Brunner, D.: Detectability of CO₂ emission plumes of cities and power plants with the Copernicus Anthropogenic CO₂ Monitoring (CO₂M) mission, *Atmospheric Measurement Techniques*, 715 12, 6695–6719, <https://doi.org/10.5194/amt-12-6695-2019>, publisher: Copernicus GmbH, 2019.



- Kuhlmann, G., Brunner, D., Broquet, G., and Meijer, Y.: Quantifying CO₂ emissions of a city with the Copernicus Anthropogenic CO₂ Monitoring satellite mission, *Atmospheric Measurement Techniques*, 13, 6733–6754, <https://doi.org/10.5194/amt-13-6733-2020>, publisher: Copernicus GmbH, 2020.
- Lack, S. A., Limpert, G. L., and Fox, N. I.: An Object-Oriented Multiscale Verification Scheme, *Weather and Forecasting*, 25, 79–92, <https://doi.org/10.1175/2009WAF2222245.1>, publisher: American Meteorological Society Section: Weather and Forecasting, 2010.
- 720 Lian, J., Wu, L., Bréon, F.-M., Broquet, G., Vautard, R., Zaccheo, T. S., Dobler, J., and Ciais, P.: Evaluation of the WRF-UCM mesoscale model and ECMWF global operational forecasts over the Paris region in the prospect of tracer atmospheric transport modeling, *Elementa: Science of the Anthropocene*, 6, 64, <https://doi.org/10.1525/elementa.319>, 2018.
- Meinshausen, M., Meinshausen, N., Hare, W., Raper, S. C. B., Frieler, K., Knutti, R., Frame, D. J., and Allen, M. R.: Greenhouse-gas emission targets for limiting global warming to 2 °C, *Nature*, 458, 1158–1162, <https://doi.org/10.1038/nature08017>, number: 7242 Publisher: Nature Publishing Group, 2009.
- 725 Menut, L., Bessagnet, B., Khvorostyanov, D., Beekmann, M., Blond, N., Colette, A., Coll, I., Curci, G., Foret, G., Hodzic, A., Mailler, S., Meleux, F., Monge, J.-L., Pison, I., Siour, G., Turquety, S., Valari, M., Vautard, R., and Vivanco, M. G.: CHIMERE 2013: a model for regional atmospheric composition modelling, *Geoscientific Model Development*, 6, 981–1028, <https://doi.org/10.5194/gmd-6-981-2013>, 2013.
- 730 Monge, G.: Mémoire sur la théorie des déblais et des remblais, *Histoire de l'Académie royale des sciences avec les mémoires de mathématique et de physique tirés des registres de cette Académie*, pp. 666–705, 1781.
- Nocedal, J. and Wright, S. J.: Large-scale unconstrained optimization, *Numerical Optimization*, pp. 164–192, publisher: Springer, 2006.
- Peyré, G. and Cuturi, M.: Computational Optimal Transport: With Applications to Data Science, *Foundations and Trends® in Machine Learning*, 11, 355–607, <https://doi.org/10.1561/22000000073>, publisher: Now Publishers, Inc., 2019.
- 735 Pison, I., Berchet, A., Saunois, M., Bousquet, P., Broquet, G., Conil, S., Delmotte, M., Ganesan, A., Laurent, O., Martin, D., O'Doherty, S., Ramonet, M., Spain, T. G., Vermeulen, A., and Yver Kwok, C.: How a European network may help with estimating methane emissions on the French national scale, *Atmospheric Chemistry and Physics*, 18, 3779–3798, <https://doi.org/10.5194/acp-18-3779-2018>, publisher: Copernicus GmbH, 2018.
- 740 Potier, E., Broquet, G., Wang, Y., Santaren, D., Berchet, A., Pison, I., Marshall, J., Ciais, P., Bréon, F.-M., and Chevallier, F.: Complementing XCO₂ imagery with ground-based CO₂ and ¹⁴CO₂ measurements to monitor CO₂ emissions from fossil fuels on a regional to local scale, *Atmospheric Measurement Techniques Discussions*, 2022, 1–44, <https://doi.org/10.5194/amt-2022-48>, 2022.
- Santaren, D., Broquet, G., Bréon, F.-M., Chevallier, F., Siméoni, D., Zheng, B., and Ciais, P.: A local- to national-scale inverse modeling system to assess the potential of spaceborne CO₂ measurements for the monitoring of anthropogenic emissions, *Atmospheric Measurement Techniques*, 14, 403–433, <https://doi.org/10.5194/amt-14-403-2021>, 2021.
- 745 Seigneur, C.: *Air Pollution: Concepts, Theory, and Applications*, Cambridge University Press, 2019.
- Solazzo, E., Crippa, M., Guizzardi, D., Muntean, M., Choulga, M., and Janssens-Maenhout, G.: Uncertainties in the Emissions Database for Global Atmospheric Research (EDGAR) emission inventory of greenhouse gases, *Atmospheric Chemistry and Physics*, 21, 5655–5683, <https://doi.org/10.5194/acp-21-5655-2021>, publisher: Copernicus GmbH, 2021.
- 750 Super, I., Dellaert, S. N. C., Visschedijk, A. J. H., and Denier van der Gon, H. A. C.: Uncertainty analysis of a European high-resolution emission inventory of CO₂ and CO to support inverse modelling and network design, *Atmospheric Chemistry and Physics*, 20, 1795–1816, <https://doi.org/10.5194/acp-20-1795-2020>, publisher: Copernicus GmbH, 2020.



- Tamang, S. K., Ebtehaj, A., van Leeuwen, P. J., Lerman, G., and Foufoula-Georgiou, E.: Ensemble Riemannian data assimilation: towards large-scale dynamical systems, *Nonlinear Processes in Geophysics*, 29, 77–92, <https://doi.org/10.5194/npg-29-77-2022>, publisher: Copernicus GmbH, 2022.
- 755 Vanderbecken, P. J.: Passive gas plume database for metrics comparison, <https://doi.org/10.5281/zenodo.6958047>, 2022.
- Varon, D. J., Jacob, D. J., McKeever, J., Jervis, D., Durak, B. O. A., Xia, Y., and Huang, Y.: Quantifying methane point sources from fine-scale satellite observations of atmospheric methane plumes, *Atmospheric Measurement Techniques*, 11, 5673–5686, <https://doi.org/10.5194/amt-11-5673-2018>, publisher: Copernicus GmbH, 2018.
- 760 Varon, D. J., Jacob, D. J., Jervis, D., and McKeever, J.: Quantifying Time-Averaged Methane Emissions from Individual Coal Mine Vents with GHGSat-D Satellite Observations, *Environmental Science & Technology*, 54, 10 246–10 253, <https://doi.org/10.1021/acs.est.0c01213>, publisher: American Chemical Society, 2020.
- Veefkind, J. P., Aben, I., McMullan, K., Förster, H., de Vries, J., Otter, G., Claas, J., Eskes, H. J., de Haan, J. F., Kleipool, Q., van Weele, M., Hasekamp, O., Hoogeveen, R., Landgraf, J., Snel, R., Tol, P., Ingmann, P., Voors, R., Kruizinga, B., Vink, R., Visser, H., and Levelt, P. F.: TROPOMI on the ESA Sentinel-5 Precursor: A GMES mission for global observations of the atmospheric composition for climate, air quality and ozone layer applications, *Remote Sensing of Environment*, 120, 70–83, <https://doi.org/10.1016/j.rse.2011.09.027>, 2012.
- 765 Villani, C.: Optimal Transport, vol. 338 of *Grundlehren der mathematischen Wissenschaften*, Springer, Berlin, Heidelberg, <https://doi.org/10.1007/978-3-540-71050-9>, 2009.